Probiotic biofilm modified scaffolds for facilitating osteomyelitis treatment through sustained release of bacteriophage and regulated macrophage polarization

Junwei Su [a,1], Yifan Wu [a,1], Zheng Wang [a], Dong Zhang [a], Xianquan Yang [b], Yong Zhao [a,*], Aixi Yu [a,**]

[a] *Department of Orthopedic Trauma and Microsurgery, Zhongnan Hospital of Wuhan University, Wuhan, 430071, Hubei, China*
[b] *Department of Orthopaedics, Gucheng County People's Hospital, Xiangyang, 441799, Hubei, China*

ARTICLE INFO

ABSTRACT

Osteomyelitis has gradually become a catastrophic complication in orthopedic surgery due to the formation of bacterial biofilms on the implant surface and surrounding tissue. The therapeutic challenges of antibiotic resistance and poor postoperative osseointegration provide inspiration for the development of bioactive implants. We have strategically designed bioceramic scaffolds modified with *Lactobacillus reuteri* (LR) and bacteriophages (phages) to achieve both antibacterial and osteogenic effects. Leveraging the tendency of bacteria to adhere to the surface of implants, bioceramics have been modified with LR biofilm to promote bone repair. The LR biofilm, sterilized by pasteurization, prevents sepsis caused by live bacteria and is biocompatible with phages. Phages, being natural enemies of bacteria, not only effectively kill bacteria and inhibit biofilm formation but also readily adsorb onto the surface of bioceramics. Hence, this scaffold, loaded with a phage cocktail, lysates specific bacterial populations, namely *Escherichia coli* (*E. coli*) and *Staphylococcus aureus* (*S. aureus*). More importantly, the inactivated LR biofilm stimulates macrophages RAW264.7 to polarize towards an anti-inflammatory M2 phenotype, creating an immune microenvironment favorable for inducing osteogenic differentiation of rat mesenchymal stem cells *in vitro*. In a rat model of infectious cranial defects, the scaffold not only effectively eliminated *S. aureus* and alleviated associated inflammation but also mediated macrophage-mediated immunoregulation, thus resulting in effective osteogenesis. Collectively, these multifunctional modified scaffolds offer an integrated approach to both bacterium elimination and bone repair, presenting a new strategy for bioactive implants in the clinical management of osteomyelitis.

1. Introduction

Osteomyelitis, a progressive inflammatory disease caused by pathogens, such as *Escherichia coli* (*E. coli*) and *Staphylococcus aureus* (*S. aureus*), is one of the most common complications after surgery and open trauma [1]. Such surgeries have a high failure rate and a high recurrence rate of infection, often requiring multiple and repeated hospitalizations to control the infection [2,3]. Antibiotic-loaded implants are a common clinical treatment [4]. However, the long-term application of broad-spectrum antibiotics can seriously damage the body's normal flora and may lead to severe fungal infections [5].

Moreover, due to the long disease cycle, prolonged antibiotic use can lead to drug resistance and increased toxic side effects [6]. With the emergence of various super-resistant bacteria, clinicians often face situations where there are no effective antibiotics available.

In order to mitigate the overuse of antibiotics and effectively treat drug-resistant bacterial infections, researchers have been exploring alternative antimicrobial agents [7]. One potential option is bacteriophages, which are natural predators of bacteria and feed on them [8,9]. Extensive research has demonstrated that phages possess potent bactericidal effects with a high level of safety, without triggering an excessive innate inflammatory response upon lysing bacteria within the human

---

body [10,11]. As early as the 1920s–1950s, scientists began investigating phage therapy for bacterial infections [12–14]. However, due to the limited antibacterial spectrum of specific bacteriophages in the past, efficient screening methods for specific pathogens were lacking, resulting in imprecise outcomes from bacteriophage therapy. Overcoming these challenges has renewed interest in utilizing phages for treating bacterial infections [15,16]. Phage therapy is still at an early stage when it comes to treating osteomyelitis [17,18]. In recent years, there have been reported cases of clinicians successfully treating patients with osteomyelitis through phage therapy after the failure of antibiotic treatment [19–21]. Bacteriophages, unlike antibiotics, are strain-specific and possess the advantages of rapid proliferation and self-limitation, which can significantly reduce the emergence of drug-resistant strains. Predictably, bacteriophages will evolve into a mature and potent weapon against infections in the future.

At present, phage therapy is mostly used in the form of injection, and the problem of whether it can be used in the form of implants to treat infectious bone defects has not been solved. Thus, the ideal implant should possess biological functions that can prevent or eliminate infections while promoting bone tissue regeneration [22–24]. Calcium phosphate-based ceramics have a mineral composition very similar to that of bone, making them good bone substitutes due to their biocompatibility and absorbability [25]. In previous studies, we found that $Ca_3(PO_4)_2$ (TCP) ceramics can naturally retain and release phage for over 6 days [26], making them a promising carrier for microbial treatment of osteomyelitis.

Probiotics, which are nonpathogenic organisms, are extensively used in managing various digestive system disorders, including inflammatory bowel disease, gastrointestinal infection, and gastrointestinal cancers, due to their immunomodulatory capabilities [27–30]. *Lactobacillus reuteri* (LR) is a resident probiotic found in the human intestine and can be commonly found in dairy products like yogurt and cheese [31]. Oral administration of LR has been demonstrated to regulate the human immune system, thereby mitigating bone loss following antibiotic usage and reducing osteoporosis risk among elderly individuals [32–35]. Probiotics like *Lactobacillus casei* and *Lactobacillus rhamnosus* have been engineered to enhance bone repair when applied to implants [36]. However, the application of LR in the treatment of infectious bone defects remains largely unexplored, particularly its coexistence with active phages has not been clearly defined yet. Interestingly, even after inactivation, probiotics still retain their functionality, which avoids biosafety concerns associated with live bacteria [37]. Moreover, unlike pathogenic bacteria counterparts, LR exhibits anti-aging effects on bones while promoting bone regeneration. Consequently, formation of a probiotic biofilm on implants may emerge as a novel biomaterial for repairing extensive bone defects.

After implants enter the body, the host's innate immune system can be activated at the interface of implanted biomaterials within hours [38]. Macrophages, among the earliest arrivals to interact with the implanted materials, which play a crucial role in initiating and mediating the host foreign body response [39]. It is well-known that macrophages exhibit remarkable plasticity and can polarize towards either M1 (proinflammatory) or M2 (anti-inflammatory) phenotypes in response to variable local microenvironments. Implantation of
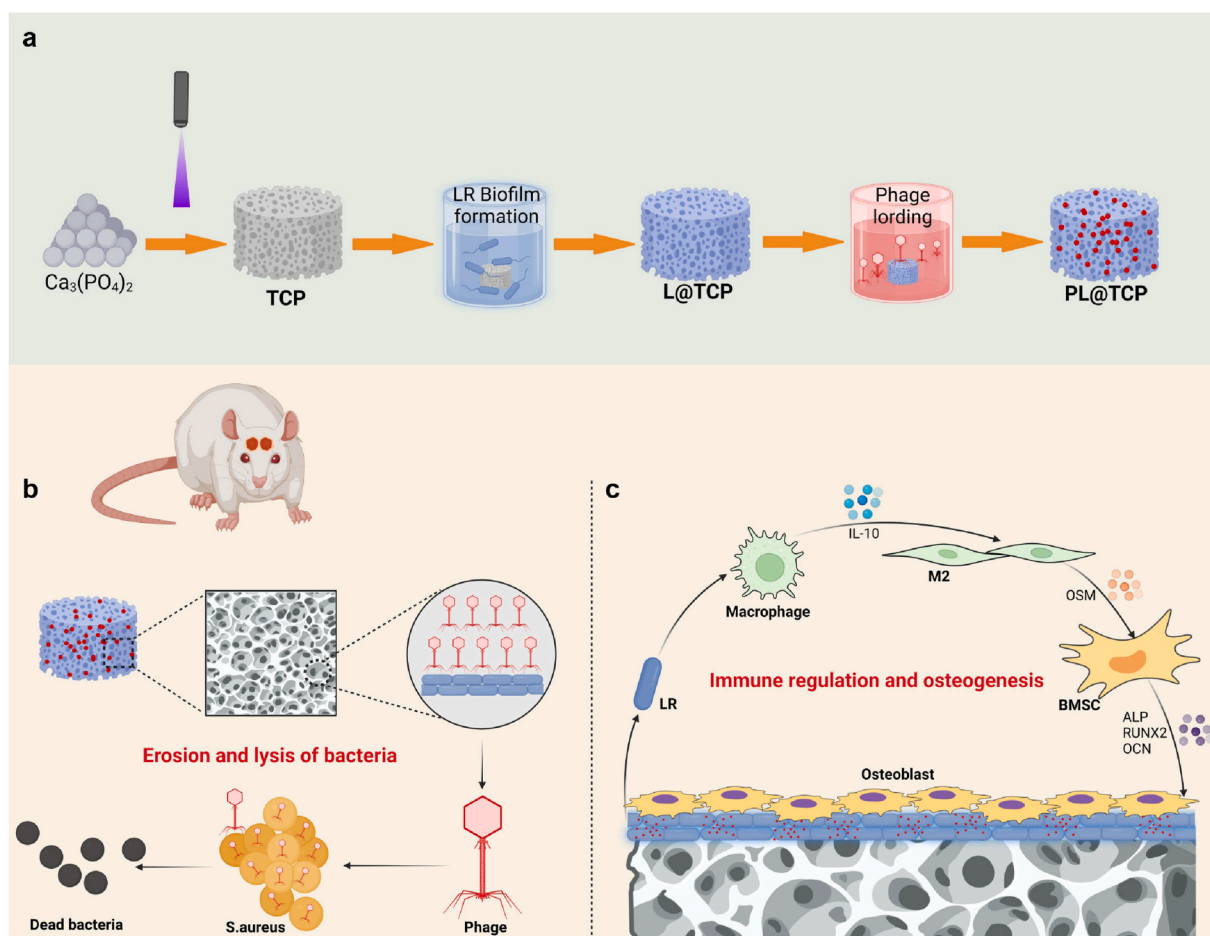
Scheme 1. Schematic presentation of probiotic biofilm modified scaffolds for facilitating osteomyelitis treatment through sustained release of bacteriophage and regulated macrophage polarization. (a) Preparation of probiotic (LR) biofilm modified TCP with phage (PL@TCP). (b) Antibacterial capability of PL@TCP. (c) Immunomodulation and osseointegration of PL@TCP.

bioceramics often promotes polarization towards an M1 phenotype, which exacerbates inflammation by releasing pro-inflammatory cytokines, leading to long-term tissue damage and impeding bone defect healing [40]. Therefore, it is highly intriguing to investigate whether LR biofilm can induce macrophage polarization towards an M2 phenotype, thereby alleviating inflammation through the production of anti-inflammatory cytokines [41], while also promoting bone healing and integration around the implant through the secretion of osteoblast-like factor [42].

Here, we constructed a calcium phosphate-based scaffold that was loaded with *E. coli* phage T4 and *S. aureus* phage K (Scheme 1a). The scaffold lysed their corresponding bacterial populations and disrupted already formed bacterial biofilms (Scheme 1b). The study also explored the role of inactivated LR biofilms in regulating macrophage polarization. Meanwhile, it is proposed that stimulating macrophages to secrete osteogenic factors may promote the osteogenic differentiation of bone mesenchymal stem cells (BMSCs) (Scheme 1c). The gene expression and signaling pathways of macrophages cultured on this scaffold were investigated by RNA-seq, verifying the anti-inflammatory effect of the material. This study enabled screening of the appropriate phage and LR concentrations to modify bioceramics for anti-infective and osseointegration functions, with the aim of curing osteomyelitis. Our study potentially provides a novel treatment for osteomyelitis.

2. Materials and methods

2.1. Preparation of bioceramics

The bioceramics were prepared following a previous study using tricalcium phosphate (TCP) [43]. Synthetic β-Ca$_3$(PO$_4$)$_2$ (β-TCP) powder was prepared via an aqueous precipitation technique using a solution of diammonium phosphate (NH$_4$)$_2$HPO$_4$ and calcium nitrate Ca (NO$_3$)$_2$·4H$_2$O, both from Sinopharm Chemical Reagent Co., Ltd [44]. The β-TCP powder was mixed with polyvinyl alcohol and placed in a circular mold. It was then sintered at 1150 °C under certain pressure. The printable slurry was prepared by mixing β-TCP powder with light-curing resin until homogenous. The pre-designed 3D structure was uploaded into the 3D printer. The resulting scaffolds were cleaned and dried before being sintered at 1150 °C to obtain the final 3D-printed TCP scaffolds [45].

2.2. Preparation and characterization of probiotic biofilm modified TCP

2.2.1. Culture of probiotics

Lactobacillus reuteri (LR, ATCC 23272) was purchased from the Guangdong Microbial Cultural Collection Center (GDMCC). LR was cultured with MRS broth at 37 °C. The LR bacterial solution was authenticated by strain identification for subsequent use.

2.2.2. Preparation of LR biofilm modified TCP

The TCP was cultured with probiotics to obtain probiotic biofilm modified TCP (L@TCP). Briefly, 100 µL of freeze-dried solution from a LR single colony was added to 10 mL of MRS broth to culture for 24 h. The TCP subjected to ultrasonic cleaning, drying and ultraviolet ray treatment was cultured with different concentrations of LR (1×10^6, 3×10^6, 1×10^7, 3×10^7, 1×10^8 CFU/mL) in 24-well plates. After 24 h of coculture, the TCPs were gently washed with sterilized PBS for three times to remove planktonic bacteria.

2.2.3. Morphological observation of LR biofilm

LR (1×10^6, 3×10^6, 1×10^7, 3×10^7, 1×10^8 CFU/mL) were cultured on TCP for 24 h. Excess LR was washed away with PBS, and the cells were fixed in 2.5 % glutaraldehyde for 2 h. The cells were then gradient-dehydrated with 30 %, 50 %, 70 %, 90 % and 100 % ethanol for 15 min each. Finally, the cell morphologies of the different samples were observed under a scanning electron microscope (SEM) from TESCAN,

Czech Republic. Additionally, an energy dispersive spectrometer (EDS) was utilized to investigate the distribution and alteration of elements.

2.2.4. Cytotoxicity of L@TCP

The *in vitro* cytotoxicity of L@TCPs was evaluated using the Cell Counting Kit-8 assay (CCK-8). Macrophages were inoculated into 24-well plates at a density of 1×10^6 cells/well in complete culture medium and cultured at 37 °C under 5 % CO$_2$ for 3 days. After culturing macrophages for 3 days, the complete medium was extracted from each well and replaced with 500 mL of fresh complete medium containing 50 mL of CCK-8 reagent. The cells were then incubated for 2 h, and the optical density (OD) at 450 nm was measured in each well.

2.2.5. Inactivation of LR biofilm by pasteurization

Separately, L@TCP was stained with SYTO9 before and after being subjected to pasteurization at a specific temperature and duration. The staining solution contained 1000 µL of PBS and 1 µL of SYTO9, and was incubated for 30 min at 37 °C. Excess SYTO9 was removed by washing the sample three times with PBS. Observations were made using laser confocal microscopy. The excitation and emission wavelengths for SYTO9 were 480 nm and 500 nm, respectively, while those for propidium iodide (PI) were 535 nm and 615 nm.

2.2.6. Effect of different concentrations of LR on macrophage polarization

To measure the cytokine of macrophages on different samples, RAW 264.7 macrophages were first cultured on different samples for 24, 48, 72 h to collect supernatants. The secretion of cytokines interleukin-6 (IL-6), tumor necrosis factor-α (TNF-α), interleukin-4 (IL-4) and interleukin-10 (IL-10) was then measured by commercial enzyme-linked immunosorbent assay (ELISA) kits (4A BIOTECH, Suzhou, China), following the manufacturer's guidance.

2.2.7. Degradation of LR biofilm on L@TCP

L@TCP was immersed in 1 mL of PBS solution and shaken at 170 rpm at 37 °C. PBS solution should be replaced every 3 days with 2 mL of fresh solution. L@TCP was incubated for 7, 14, 21 and 28 days, and SEM images of LR biofilm on L@TCP were collected at each time point.

2.3. Preparation and characterization of bacteriophage modified L@TCP

2.3.1. Culture of bacterial strains and bacteriophages

Staphylococcus aureus (*S. aureus*) and *Escherichia coli* (*E. coli*) were obtained from the American Type Culture Collection (ATCC). Bacteriophage (phage) K and phage T4 were also obtained from ATCC. The bacteria were grown in Lysogeny Broth (LB) at 37 °C with shaking at 170 rpm (ZWY - 2102C, Zhicheng, China). LB medium was solidified by adding 15 g/L agar when necessary. The T4 phage stock was prepared by infecting *E. coli*, while the K phage stock was prepared by infecting *S. aureus*. After overnight enrichment in a liquid LB medium at 37 °C, chloroform was added to both phages, and the bacterial debris was removed by centrifugation (30 min at 3000 g at 4 °C). To quantify the phages, we plated 10^6-fold diluted phages and 10^8 CFU/mL bacteria on an R-medium agar plate. The R-medium agar plates contained bactotryptone (10 g/L), yeast extract (1 g/L), NaCl (8 g/L), and agar (12 g/L). We used 5 mL of R-Top medium (Bactotryptone 10 g/L, yeast extract 1 g/L, NaCl 8 g/L, and agar 8 g/L) and incubated the plates at 37 °C. After 24 h, we counted the lysis plaques to estimate the number of pfu (plaque forming unit)/mL.

2.3.2. Quantification of phages loaded in TCP scaffolds

To quantify the phages loaded in TCPs, the phages were removed from TCPs by washing them with a desorption buffer (0.15 M NaCl, 200 mM NaH$_2$PO$_4$, pH 7) for 1 h at 37 °C with shaking at 170 rpm. After recovering the eluate, TCPs were washed twice with stripping buffer (0.15 M NaCl, 1 M NaH$_2$PO$_4$, pH 7) for 1 h at 37 °C while shaking at 170 rpm. The eluates were collected and pooled. Phage enumeration was

performed as described previously. To confirm that all phages were recovered, a final wash with stripping buffer was performed, and the resulting eluate was tested for optical density at 269 nm (OD_{269}). The OD_{269} was close to zero, indicating that nearly all phages were harvested. To further confirm this, the eluate was tested using a lysis plaque assay, which showed no presence of lysis plaques (pfu) in the last eluate, confirming that all phages had been desorbed.

2.3.3. Preparation of phage modified L@TCP

To load phages on the L@TCP, Ceramic pellets were placed in 24 well plates, covered by 2 mL of phage suspension stock (1×10^6, 1×10^7, 1×10^8, 1×10^9, 1×10^{10} CFU/mL for phage T4 or K suspension) and stored 24 h at 4 °C. After washing 3 times with PBS, PL@TCP were obtained. These were named T4(10^6)L@TCP, T4(10^7)@TCP, T4(10^8)@TCP, T4 (10^9)@TCP, T4(10^{10})@TCP, K(10^6)L@TCP, K(10^7)@TCP, K(10^8)@TCP, K(10^9)@TCP and K(10^{10})@TCP.

2.3.4. Antimicrobial activity of different concentrations of phage T4/K

T4L@TCP was tested for its antimicrobial activity against *E. coli* and KL@TCP was tested for its antimicrobial activity against *S. aureus*. *E. coli* and *S. aureus* were amplified using LB broth and diluted to a concentration of 10^8 CFU/mL. Different scaffolds were added to a 24-well plate containing 1 mL of PBS. A pipette gun was used to add 10 μL of bacterial solution (10^8 CFU/mL) to the surfaces of the TCP samples. For the negative control group, a bacterial suspension of 10 μL (10^8 CFU/mL) was added to the 24-well plate and re-suspended with 1 mL sterile PBS. The 24-well plates were then incubated at 37 °C in a biochemical incubator. After 6 h, the plates were removed, and the suspended bacteria were extracted by repeatedly blowing with a pipette gun. Subsequently, 10 μL of the bacterial resuspension was drawn and diluted to 1 mL, and evenly coated onto an LB agar plate. The LB agar plate was cultured in a biochemical incubator at 37 °C for 18–24 h. The number of colony-forming units on the LB agar plate was calculated, and the results were expressed as CFU. The antibacterial capacity of PL@TCP was then determined. The antimicrobial activity of PL@TCP is expressed by the following formula: Antimicrobial activity of PL@TCP (%) = ((Control CFU - Specific ager plate CFU)/Control CFU) × 100 %.

2.3.5. Cytotoxicity and lytic kinetics of PL@TCP

Next, the cytotoxicity of PL@TCP was evaluated *in vitro* using the CCK-8 reagent, following the method described above. Then, bacterial lysis assays with P@TCP in liquid medium. Bacterial growth was monitored by optical density at 600 nm (OD_{600}) in a microplate reader (FC, ThermoFisher, USA). Before adding TCP pellet, *E. coli* or *S. aureus* were grown in 30 mL LB at 37 °C at a starting OD_{600} of 0.03 with shaking. When the culture reached an OD_{600} of 0.1, P@TCP samples were immersed in culture tubes. Growth was monitored by OD_{600} either until complete lysis of the bacteria or until the stationary phase. When necessary, *E. coli* or *S. aureus* were enumerated by plating serial dilutions and allowing them to grow overnight on solid LB medium, using the different colony phenotypes of both species for identification.

2.3.6. Retention of phages on L@TCP over 1 month

PL@TCP was immersed in 1 mL of LB solution and shaken at 170 rpm at 37 °C. The LB solution should be replaced every 3 days with 2 mL of fresh solution. The material was incubated for 0, 3, 6, 9, 12, 15, 18, 21, 24, 27 and 30 days, and the phage (T4 or K) in the LB solution was quantified at each time point. The rate of phage release is expressed by the following formula: The rate of phage release (%) = (Each time point PFU/Day 0 PFU) × 100 %.

2.4. Antimicrobial activity of PL@TCP

2.4.1. Staining of live and dead bacteria

S. aureus and *E. coli* were cultured in LB broth. The bacterial solution was then diluted to a concentration of 10^8 CFU/mL. Next, 1 mL of the bacterial suspension at 10^8 CFU/mL was added to a sterile centrifuge tube. Subsequently, either TCP, L@TCP, P@TCP, or PL@TCP was added to the tube, while 100 μL of PBS was added to the control group. The centrifuge tubes were incubated in a bacterial shaker at 37 °C for 6 h. Afterward, 100 μL of the bacterial suspension was pipetted and mixed with an equal volume of staining solution containing 12 μM SYTO9 and 60 μM PI. The bacterial suspension not co-cultured with TCP was stained with SYTO9 and PI solution in the negative control group. The mixture was incubated for 15 min at room temperature, protected from light. Place 5 μL of the sample between a microscope slide and coverslip, then observe using an orthogonal fluorescence microscope. Excitation wavelength for SYTO9 should be 480 nm, with an emission wavelength of 500 nm. For PI, the excitation wavelength should be 535 nm, and the emission wavelength should be 615 nm.

2.4.2. Crystal violet staining of biofilms

Coverslips were placed in 6-well plates, and 200 μL of *E. coli* and *S. aureus* suspension (1×10^8 CFU/mL) in LB medium was inoculated onto the coverslips in the center. Then, 2 mL of fresh LB was added. The inhibition group was incubated with PL@TCP and bacteria for 48 h simultaneously, while the untreated biofilm was used as the negative control group. The destruction group was statically incubated with bacteria for 48 h. Then, it was treated with PL@TCP, while 100 μL PBS was added to the negative control group. After incubation of the biofilm, the coverslips were removed, and the biofilm was lightly treated with sterile PBS buffer three times to remove unattached bacteria. The biofilm was stained with 1 ml of 0.1 % crystal violet solution at 37 °C for 30 min. After staining, rinse the sample three times with PBS and capture images once they have dried. The biofilm was dissolved in 95 % ethanol for 5 min, and the optical density (OD) at 560 nm (OD_{560}) was measured using a microplate reader (FC, ThermoFisher, USA). The percentage of inhibition and destruction was calculated using OD_{560} according to the following formula: Biofilm clearance (%) = ((OD Control group - OD experimental group)/OD Control group) × 100 %.

2.4.3. Microscopic observation of biofilms

Bacterial biofilms were prepared as described previously. Next, 1000 μL PBS with 1 μL SYTO9 was added and incubated at 37 °C for 30 min. The staining solution was then removed, and the biofilm was gently washed three times with PBS to remove excess SYTO9. The cover glass on the biofilm was then removed and placed on the slide to seal the film. The surface and lateral thickness of the bacterial biofilm were observed using a laser confocal microscopy. The SYTO9 excitation wavelength is 480 nm, and the emission wavelength is 500 nm.

2.5. PL@TCP co-cultured with RAW264.7 macrophages

2.5.1. Macrophage response to different scaffolds in vitro

To investigate how PL@TCP activates macrophages, RAW 264.7 macrophage cells were cultured in an incubator at 37 °C with a 5 % CO_2 atmosphere. RAW 264.7 macrophages were cultured in Dulbecco's modified Eagle's medium (HyClone, USA) containing 1 % penicillin-streptomycin solution (Gibco, USA) and 10 % fetal bovine serum (FBS) (Gibco). The macrophages (1×10^6 cells per well) were exposed to TCP, P@TCP, L@TCP and PL@TCP for 72 h. The control group was the blank group.

2.5.2. Immunofluorescence staining

RAW 264.7 macrophages were cultured on various samples for 72 h. Afterward, they were fixed with 4 % paraformaldehyde for 20 min, permeabilized with 0.25 % Triton X-100 for 20 min, and then blocked with 1 % bovine serum albumin for 1 h. The cells were then incubated with primary antibodies against CD206 (Abcam) and CD86 (Abcam) at a 1:100 dilution at 4 °C overnight. Following primary antibody incubation, the cells were incubated with either Alexa Fluor 488 conjugate anti-mouse or Alexa Fluor 594 conjugate anti-mouse secondary antibody

for 30 min. This was followed by 5 min of nuclear staining with 4′,6-diamidino-2-phenylindole (DAPI). The immunofluorescence-stained cells were visualized using a laser scanning confocal microscope (Leica STELLARIS 5 SR, German).

2.5.3. Quantitative real-time polymerase chain reaction

The macrophages (1×10^6 cells per well) were cultured with TCP, P@TCP, L@TCP, and PL@TCP for 72 h. The control group was the blank group. The total RNA was extracted and reversely transcribed to complementary DNA by a PrimeScript RT Master Mix. RT-PCR analysis was examined using a Bio-Rad RT-PCR system. The expression levels of TNF-α, IL-10, and oncostatin M (OSM) from macrophages were tested. The glyceraldehyde-3-phosphate dehydrogenase (GAPDH) were respectively used as internal control genes. Table S2 shows the primer sequences of the tested genes.

2.5.4. Western blotting analysis

After treating the cells as previously described, proteins were extracted using RIPA buffer. 40 μg of lysate proteins were separated by SDS-PAGE and transferred to PVDF membranes. The PVDF membranes were blocked with 5 % non-fat milk for 60 min and incubated with primary antibodies overnight at 4 °C. Then, the membranes were washed and incubated with a horseradish peroxidase-labeled secondary antibody for 30 min at room temperature. The protein bands were detected using a chemiluminescence system. The samples tested were different scaffolds, with the control group being an unstimulated control. Finally, protein expression was measured using enhanced chemiluminescence reagents, with GAPDH protein used as a reference. The bands were imaged, and their optical density was quantified using ImageJ software (National Institutes of Health, USA).

2.6. BMSCs co-cultured with macrophage cytokines from immune microenvironment of PL@TCP

2.6.1. In vitro immunoregulation of osteogenesis of BMSCs

The rat bone marrow mesenchymal stem cells (BMSCs) were extracted from the bone marrow cavity of 4-week-old Sprague Dawley (SD) rats and co-cultured with α-MEM supplemented with 10 % FBS and 1 % penicillin-streptomycin solution. To investigate the regulatory role of RAW 264.7 macrophages in response to different samples on BMSCs osteogenesis, RAW 264.7 macrophages were cultured on different samples at 37 °C for 72 h to collect supernatants of macrophages (CM). The third passage BMSCs were seeded in different CM and cultured in the same medium described above but supplemented with supernatant from macrophages at a ratio of 1:1. After 3 days coculture, α-MEM was removed and washed with PBS for three times. Then, samples were fixed with 4 % paraformaldehyde for 15min, followed with staining with rhodamine-phalloidin to visualize the cytoskeletons. For osteogenic differentiation, BMSCs were seeded into 6-cell plate and cultured with α-MEM. After co-culture for 48h, the medium was changed every other day with a 1:1 mixture of CM and fresh α-MEM supplemented with 10 mmol/L β-disodium glycerophosphate, 50 μg/ml ascorbic acid and 10 nmol/L dexamethasone.

2.6.2. ALP activity

We performed ALP staining to assess the formation of ALP in BMSCs cultured on various samples using supernatants collected on days 3 and 7. After culturing the cells for a specific period, we gently washed them with PBS three times. Then, we fixed the cells with 4 % para-formaldehyde for 20 min. Next, we applied a BCIP/NBT alkaline phosphatase chromogenic kit (Beyotime, Shanghai, China) for 30 min at room temperature. After staining, the BMSCs were washed with PBS and observed using a microscope (ICX41, SOPTOP, China).

2.6.3. Alizarin Red staining

To assess the mineralization tendency of BMSCs cultured on various

samples, we used the collected supernatants at days 14 and 21. We performed Alizarin Red staining on the cells. After culturing the cells for a specific period, we gently washed the cell medium with PBS three times. Then, we fixed the cells with 4 % paraformaldehyde for 20 min, then stained them with Alizarin Red S for 30 min at room temperature. Finally, we rinsed with PBS to remove excess stain. Following the completion of staining, a microscope (ICX41, SOPTOP, China) were taken and microscopic observations were made to evaluate the impact of PL@TCP on the osteogenic differentiation of BMSCs.

2.6.4. Quantitative real-time polymerase chain reaction

BMSCs (1×10^6 cells per well) were treated with collected supernatants of macrophages (CM) conditioned with Control, TCP, P@TCP, L@TCP and PL@TCP (72 h), respectively, for 7 days. The corresponding groups were set as $CM^{Control}$, CM^{TCP}, $CM^{P@TCP}$, $CM^{L@TCP}$ and $CM^{PL@TCP}$. The culture medium was changed every 2 days. The expression levels of osteogenesis-related genes, alkaline phosphatase (ALP), runt-related transcription factor 2 (RUNX2) and osteocalcin (OCN) from BMSCs were tested. The β-actin were respectively used as internal control genes. Table S3 shows the primer sequences of the tested genes.

2.7. BMSCs directly co-cultured with PL@TCP

BMSCs directly co-cultured with PL@TCP, and then without or with the addition of the $CM^{PL@TCP}$. ALP staining after 7 days and alizarin Red staining after 21 days.

2.8. Transcriptome sequencing and data analysis

Two milliliters of macrophage cell suspension (1×10^4 cells/ml) were cultured with various samples in a six-well plate for 72 h. The macrophages were then lysed using Trizol reagent (Beyotime Biotechnology), and the resulting cell lysates were stored at −80 °C before sequencing. RNA sequencing was performed using an Illumina HiSeq X10 (Illumina, USA). The gene expression value was transformed as log10[TPM (Transcripts Per Million) + 1]. The GO and KEGG pathway enrichment analyses were conducted using the free online platform provided by Majorbio (www.majorbio.com). The process for BMSCs was identical to that of macrophages, with no additional instructions required.

2.9. In vivo anti-infection and osteogenesis study

The Animal Experimental Ethics Review Committee of Zhongnan Hospital of Wuhan University approved all animal experiments (approval number: ZN2023191), which were conducted in accordance with the National Research Council's Guidelines for the Care and Use of Experimental Animals. The cranial defect (diameter = 4.5 mm, both sides) was filled with a gelatin sponge containing a bacterial solution of 10^7 CFU/mL of S.aureus [46,47]. Forty male rats with infected cranial defects were randomly divided into five groups (n = 8): a control group, a group treated with TCP, a group treated with L@TCP, a group treated with P@TCP, and a group treated with PL@TCP. Two weeks after the first surgery, debridement and implantation of different biomaterials were performed. Two weeks after treatment, general photographs of the surgical site was obtained from three rats in each group. Four weeks after treatment, half of the rats in each group were euthanized. Cranial specimens were collected and scanned by micro-CT, and 2 mm × 1 mm granulation tissue was harvested from the defect. The specimens were homogenized in 10 mL sterile saline for 5 min. A volume of 100 μL of the resulting solution was seeded onto LB agar plates and incubated at 37 °C for 24 h, after which viable counts were collected. The resulting Micro-CT data were analyzed using image J software to determine the proportion of newly formed bone. Next, all samples were fixed in a 10 % neutral formalin solution for one week and decalcified with a 17 % EDTA solution for five weeks before being processed into paraffin

sections. Coronal sections were prepared at 4 μm and subjected to histopathological staining using H&E, Masson's reagent, as well as immunohistochemistry (Gimesa, RUNX2, bone morphogenetic protein 2 (BMP-2), CD146) and immunofluorescence (OCN, osteopontin (OPN), CD11b, CD86, CD206). After eight weeks of biomaterial implantation, the rats exhibited normal physiological conditions. The skull specimens were scanned using Micro-CT and analyzed histologically with H&E and Masson staining.

2.10. Statistical analysis

Each experiment was evaluated using the mean values ± standard deviation from at least three tests. Data analysis was performed using GraphPad Prism version 9. One-way ANOVA was used to analyze data from multiple groups, and two-tailed Student's t-test was used to compare two groups. *P*-value of less than 0.05 was considered statistically significant.

3. Results and discussion

3.1. Preparation and characterization of probiotic biofilm modified TCP

TCP artificial bone is a common implant for the clinical treatment of bone defects (Fig. 1a) [48]. The easy adhesion of bacteria to the implant, leading to rapid biofilm formation, poses a significant challenge in the treatment of osteomyelitis. In contrast, we have opted for probiotics, which are non-pathogenic bacteria, as a means to enhance artificial bone functionality. Probiotics have better biosafety and osteogenic properties, while non-probiotics such as *S. aureus* have biosecurity threats and negligible osteogenic capacity. LR is a representative probiotic, we select LR to improve TCP bioactive ceramics [49,50]. Currently, no studies have explored the relationship between the loading amount of probiotics and their bioactivity. A concentration gradient ranging from 1×10^6 CFU/mL to 1×10^8 CFU/mL of LR was established, and TCP was immersed to create the probiotic biofilm. To verify the number of LR attached to LR-coated TCP (L@TCP), LR is recovered in two batches using continuous oscillation. The plates were then coated with a 10^6-fold dilution (Fig. 1b). The number of LR growing on TCP was calculated to be 3.0×10^6, 9.2×10^6, 4.4×10^7, 6.1×10^7, and 1.0×10^8 CFU with increasing immersion concentration (Fig. 1c). SEM observations showed that the distribution of LR at low concentrations was more dispersed and did not achieve the ideal state of biofilm formation, but an LR immersion concentration greater than 10^7 CFU/mL was sufficient (Fig. 1d). The entry of viable bacteria into the bloodstream can cause sepsis. Therefore, to mitigate biosafety concerns of implants *in vivo*, the biofilm was inactivated by pasteurization based on published literature [51]. Fortunately, SEM showed that the LR remained intact in the skeleton and pasteurization did not lyse the biofilm (Fig. 1e). Cell viability of LR was examined using live/dead staining, which showed that pasteurization could completely inactivate the LR (Fig. 1f). This approach ensures better *in vivo* biocompatibility and suggests great potential in biomedical applications. Elemental distribution was also examined by energy dispersive spectroscopy (EDS). The presence of carbon and nitrogen elements, consistent with the bacterial skeleton distribution, visualized by EDS mapping analysis also indicated successful adhesion of LR (Fig. 1g).

To verify its immunomodulatory capacity, co-culture of L@TCP with macrophages was continued using the above grouping. After 72 h, the cytotoxicity of L@TCP was determined by CCK-8. LR-soaked concentrations below 10^7 CFU/mL showed no significant difference in macrophage viability compared to the control group (Fig. 1h). While the groups with 3×10^7 and 10^8 showed some cytotoxicity, the cell viability still exceeded 80 %, which is within the acceptable range. This phenomenon may be related to the production of lactic acid and hydrogen peroxide by probiotics. The ELISA analyses showed the expression of M1 and M2 macrophage-associated genes. From the overall trend, L@TCP

groups showed decreased expression levels of M1-related genes (IL-6 and TNF-α) but increased expression levels of M2-related genes (IL-4 and IL-10) compared to non-LR groups (Fig. 1i and j). When analyzed over time, every 24 h, the expression of IL-6 and TNF-α was increased and the expression of IL-4 and IL-10 was decreased in non-LR groups. The L@TCP groups showed the opposite trend: the anti-inflammatory cytokines were increased with increasing LR concentration. A perfect implant must balance cytotoxicity and efficacy. Here, we chose the L(10^7)@TCP group for the post-treatment experimental design because of its safe biocompatibility and strong immunomodulatory ability against macrophages. In addition, SEM images illustrated the long-term stability of the LR biofilm on the L@TCP (Supplementary Fig. 1). The integrity of the LR biofilm didn't change significantly after 1 week. The integrity was reduced by about half after 2 weeks, and there was essentially no LR biofilm after 4 weeks. The results demonstrated that L@TCP exhibited the most promising functional potential within 1 week due to the integrity of the LR biofilm. As the LR biofilm degraded, the efficacy of L@TCP diminish.

3.2. Preparation and characterization of phage modified L@TCP

Most phages can be classified as being lytic or temperate [52]. Lytic phages kill a very high proportion of the bacterial cells they infect, whereas a high proportion of cells survive after temperate phages infection. Therefore, lytic phages are more suitable for therapeutic consideration than temperate phages. In particular, we have selected two types of lytic phages, *E. coli* phage T4 and *S. aureus* phage K [53,54]. Phage T4 lyses *E. coli* specifically and rapidly [55]. Phage K lyses *S. aureus* exclusively and efficiently [56]. PL@TCP was prepared by the immersion because phages are easily adsorbed onto TCP. For medical use, the phage loading process must be highly reproducible. It is important to investigate the number of phages that adhere to the TCP at varying concentrations. Therefore, the amount and variability of phage T4 and K encapsulated on L@TCP were determined separately. After coating on TCP particles, phages could not be counted in situ. Therefore, phages were isolated from PL@TCP by multiple washes and the number of loaded phages was counted for phage T4 or K on *E. coli* or *S. aureus*, respectively. The quantity of phage plaques increases proportionally with the immersion concentration, ranging from 10^6 CFU/mL to 10^{10} CFU/mL. The plate was covered with a bacterial lawn that became transparent due to phage-induced lysis (Fig. 2a and b), demonstrating that inactivated LR biofilms are not biotoxic to phages. The double agar plate method revealed a significant difference in the number of T4 and K phages counted, indicating differing interaction properties of the TCP material between the phages (Fig. 2c, d and Table S1). Phages have good biosafety, and we co-cultured macrophages with the PL@TCP groups. As shown in Fig. 2(e and f), the cytocompatibility results were consistent with previous reports. Phages can rapidly and specifically lyse bacteria. To validate the bactericidal ability of T4L@TCP or KL@TCP, *E. coli* or *S. aureus* (10^8 CFU/mL) were selected. After 6 h, the number of colonies on the plates decreased as the phages increased (Fig. 2g, h and Supplementary Fig. 2).

Bacterial optical density (OD) values were measured every 30 min by spectrophotometry. T4L@TCP groups or KL@TCP groups inhibited the growth of *E. coli* (Fig. 2i) or *S. aureus* (Fig. 2j) and caused a clear inflection point in the bacterial growth curve at 240 min. At 360 min, the OD values for the high concentration group were below 0.1, which is consistent with the plate counts. The different trends in the antibacterial effects of the two phages on the bacteria indicate differences in their lysing ability. Interestingly, when combined with plate counts and OD values, the antimicrobial capacity of phage T4 or K was nearly as strong in groups 10^9 and 10^{10}. As a result, the lowest effective concentration of T4(10^9)L@TCP and K(10^9)L@TCP was chosen for subsequent experiments. Phage retention and release on PL@TCP was measured. Phages collected from the wash were quantified every three days (Supplementary Fig. 3). The curve of release demonstrates an initial
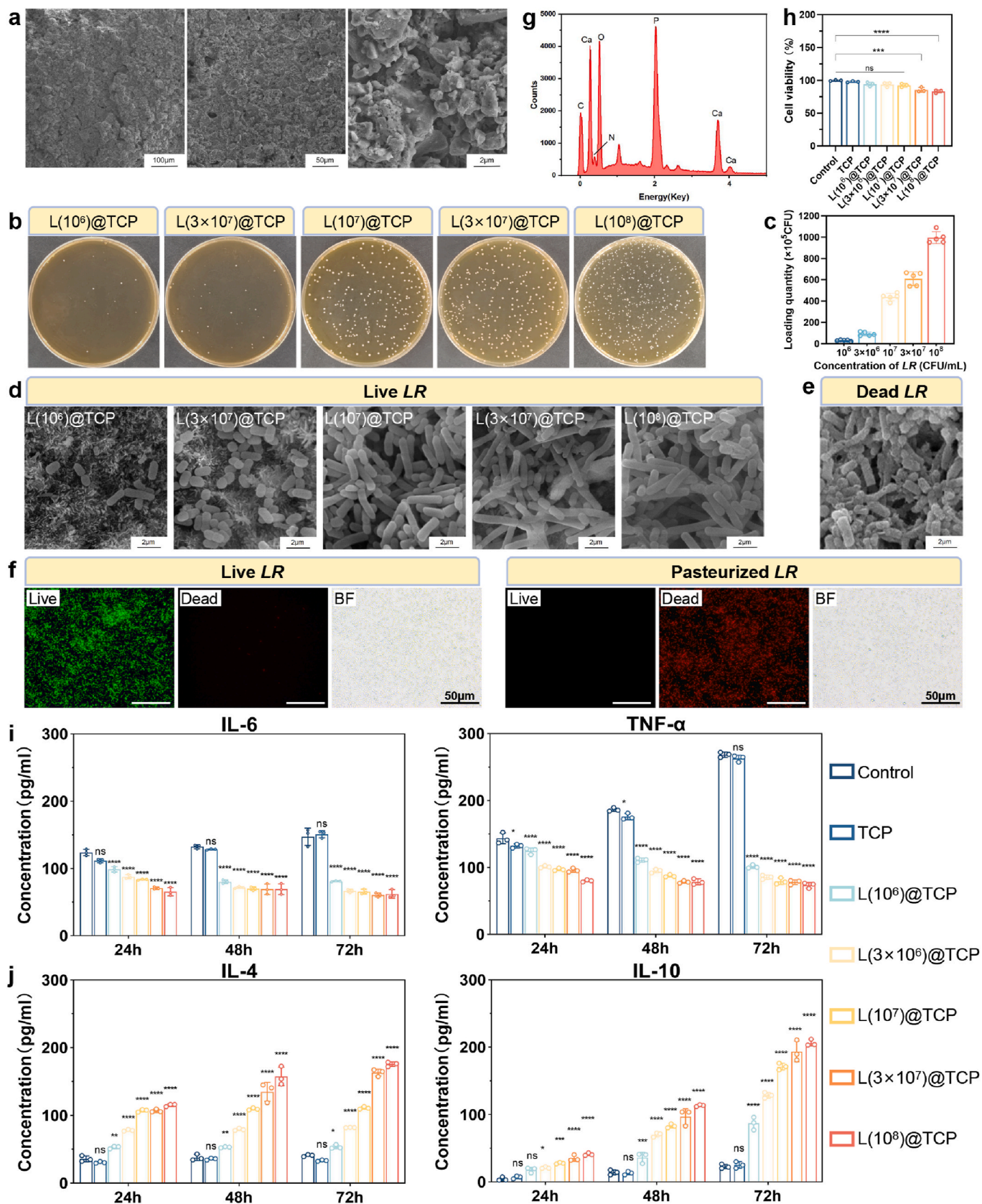
Fig. 1. Characterization of probiotic biofilm modified TCP. (a) SEM images of TCP. (b) LR on MRS agar plates after elution and dilution. Different concentrations (1 $\times 10^6$, 3×10^6, 1×10^7, 3×10^7, 1×10^8 CFU/mL) of LR loaded in TCP for 24 h. (c) Quantitative analysis of LR loaded in TCP based on MRS agar plates. (d) SEM images of LR biofilm modified TCP (L@TCP). (e) SEM images of LR biofilm with pasteurization. (f) Live/dead staining for LR received with or without pasteurization. (g) The quantification of elements on L@TCP. (h) CCK-8 assays of bioactivities of macrophages cultured on L@TCPs on day 3. (i) ELISA analyses of M1-related cytokines IL-6 and TNF-α. (j) ELISA analyses of M2-related cytokines IL-4 and IL-10. *$P < 0.05$, **$P < 0.01$, ***$P < 0.001$, ****$P < 0.0001$.
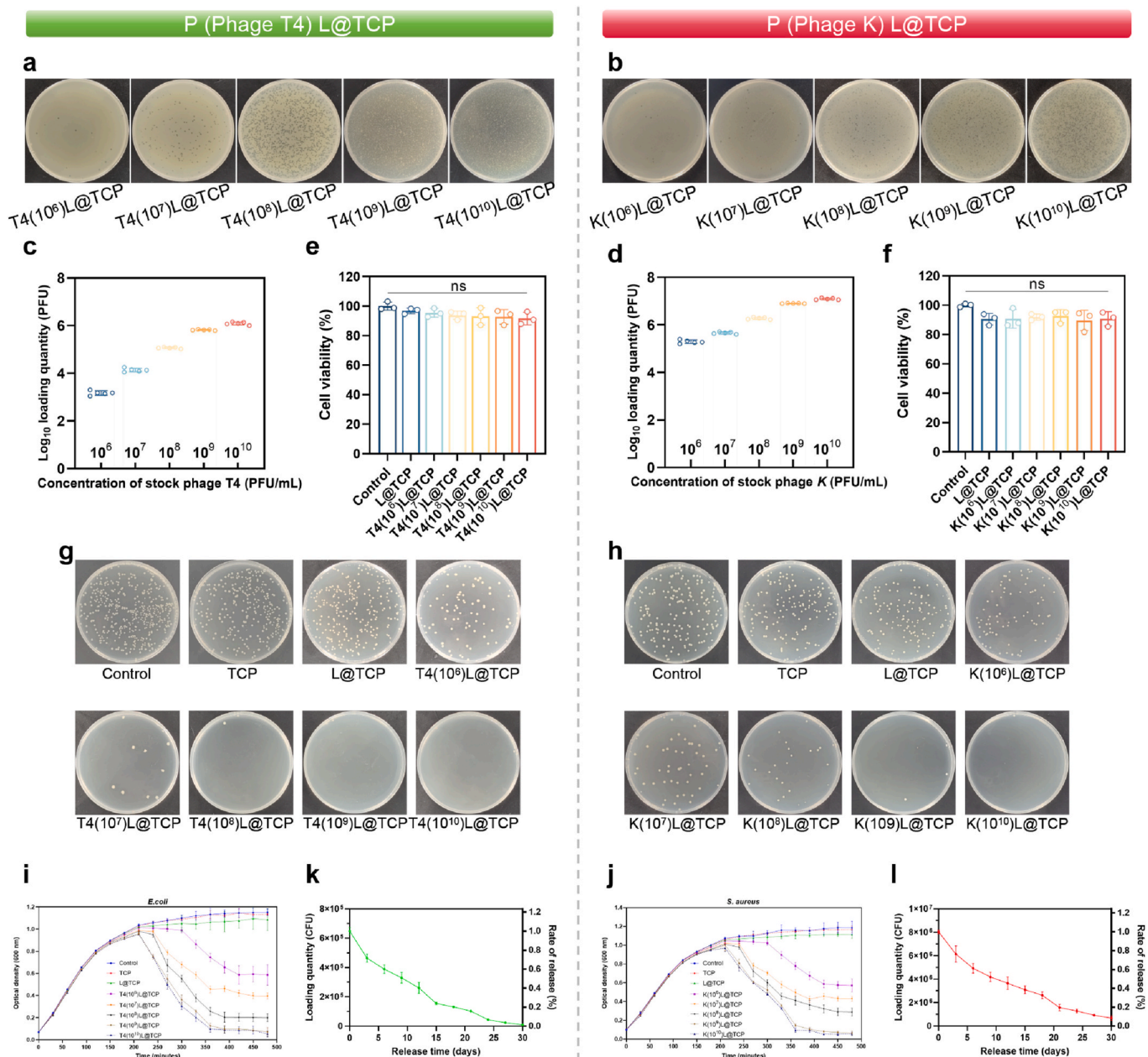
Fig. 2. Characterization of phage modified L@TCP (PL@TCP). Plaques of phage T4 and phage K on double AGAR plates by elution and dilution. Different concentrations (1×10^6, 1×10^7, 1×10^8, 1×10^9, 1×10^{10} CFU/mL) of (a) Phage T4 or (b) phage K loaded in L@TCP. Quantitative analysis of (c) phage T4 and (d) phage K loaded in TCP based on Plaques. CCK-8 assays of bioactivities of macrophages cultured on (e) T4L@TCPs and (f) KL@TCPs on day 3. Antibacterial effects on (g) *E.coli* cultured with T4L@TCPs and (h) *S.aureus* cultured with KL@TCPs after 6 h. Lytic kinetics of (i) *E.coli* cultured with T4L@TCPs and (j) *S.aureus* cultured with KL@TCPs after 8 h. Retention and release of (k) phage T4 and (l) phage K on PL@TCP for 30 days.

rapid decline followed by a deceleration. Phage T4 was released by about 50 % on day 9, less than 20 % remained on day 15, and almost none on day 30 (Fig. 2k). Phage K was released by more than 50 % on day 12, less than 20 % remained on day 21, and close to 10 % remained on day 30 (Fig. 2l). The long-term retention of phage ensures its enduring antimicrobial efficacy.

3.3. PL@TCP promoted antibacterial capability in vitro

Phages rapidly invade bacteria, replicate within the host bacterium, and ultimately cause lysis. The survival of typical bacteria in osteomyelitis can be observed through live-dead stained images in the presence or absence of phages. Fig. 3a shows that in the presence of phage, *E. coli* is visible as red cells and less green cells at 6 h. Interestingly, the

inactivated LR biofilm exhibited slight antimicrobial capacity. Hydrogen peroxide and lactate produced by probiotic bacteria that adhere to TCP might be linked to the observed antimicrobial effects. The response of *S. aureus* was similar (Fig. 3b). The merged images showed predominantly green cells in the control and TCP groups, whereas the P@TCP and PL@TCP groups exhibited fields of yellow cells. The L@TCP group was intermediate.

In osteomyelitis, bacterial biofilms pose a challenge for treatment due to barriers to drug entry and the presence of dormant sites for bacteria [57]. The key to controlling the infection is to inhibit and disrupt the biofilm. The PL@TCP is tested for the ability to inhibit biofilm by co-culturing with bacteria for 48 h, and also for the ability to disrupt biofilm by treating pre-cultured bacteria for 24 h after 48 h of growth. Crystal violet staining revealed that P@TCP and PL@TCP
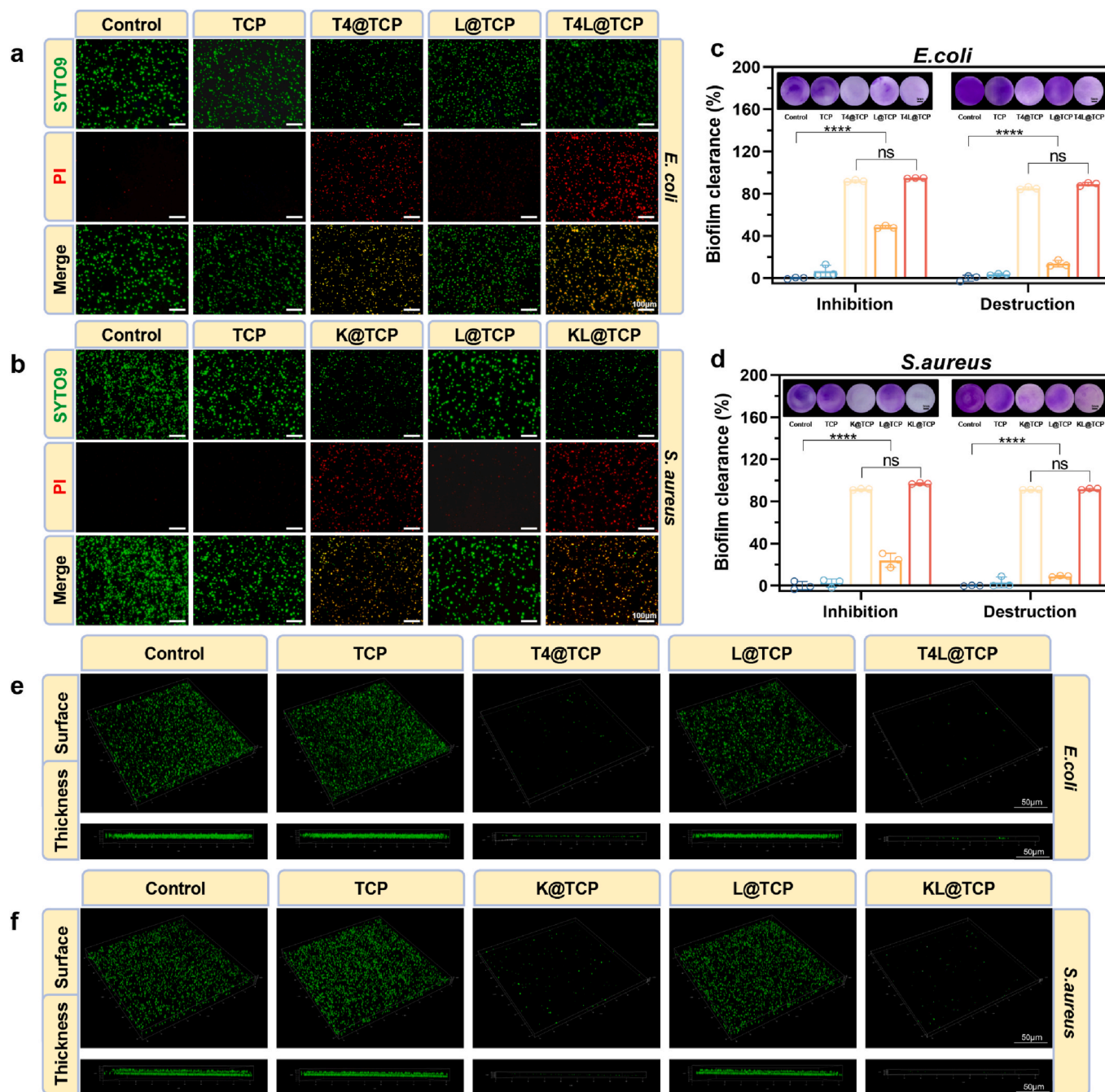
Fig. 3. Antimicrobial and biofilm lysis capabilities of P(T4/K)L@TCP *in vitro*. (a) Live (green)/dead (red) staining of *E. coli* cultured with T4L@TCP after 6 h. (b) Live (green)/dead (red) staining of *S. aureus* cultured with KL@TCP after 6 h. (c) Crystal violet staining of *E. coli* biofilm and biofilm clearance cultured with T4L@TCP. (d) Crystal violet staining of *S. aureus* biofilm and biofilm clearance cultured with KL@TCP. CLSM surface and thickness images of (e) *E. coli* and (f) *S. aureus* biofilm. ****$P < 0.0001$.

significantly inhibited and destroyed the biofilms of *E. coli* (Fig. 3c) and *S. aureus* (Fig. 3d). This was attributed to the secretion of extracellular matrix hydrolase, bacterial cell membrane lyase, and bacterial cell wall lyase by the phages. After 48 h of unrestricted growth, the biofilm becomes impenetrable, and complete lysis is extremely difficult in a short period. However, the phage could still destroy most of the biofilm. The results indicate that treating osteomyelitis is difficult once it develops in the clinic, as shown by the little disruption of the biofilm in the control group. Laser confocal revealed that the bacterial biofilm is a multilayered stack, with the biofilm of *S. aureus* being denser than that of *E. coli*. PL@TCP was most effective in disrupting the biofilm, as demonstrated by the surface view and thickness (Fig. 3e and f).

3.4. PL@TCP activated macrophages

The key hypothesis of this study is that LR can activate macrophages. To investigate the effect of PL@TCP on macrophages, RAW 264.7 macrophages were seeded on the material for 72 h. We stained the macrophages with 4′,6-diamidino-2-phenylindole (for nucleus visualization) and fluorescein isothiocyanate (FITC)–conjugated Phalloidin (for F-actin) to observe their morphologies (Fig. 4a). Upon stimulation with LR biofilm, macrophages underwent a transformation from a round and clustered morphology to an elongated cell shape with long pseudopods. To verify this, immunofluorescent staining was applied to explore whether LR biofilm can induce macrophage polarization. We
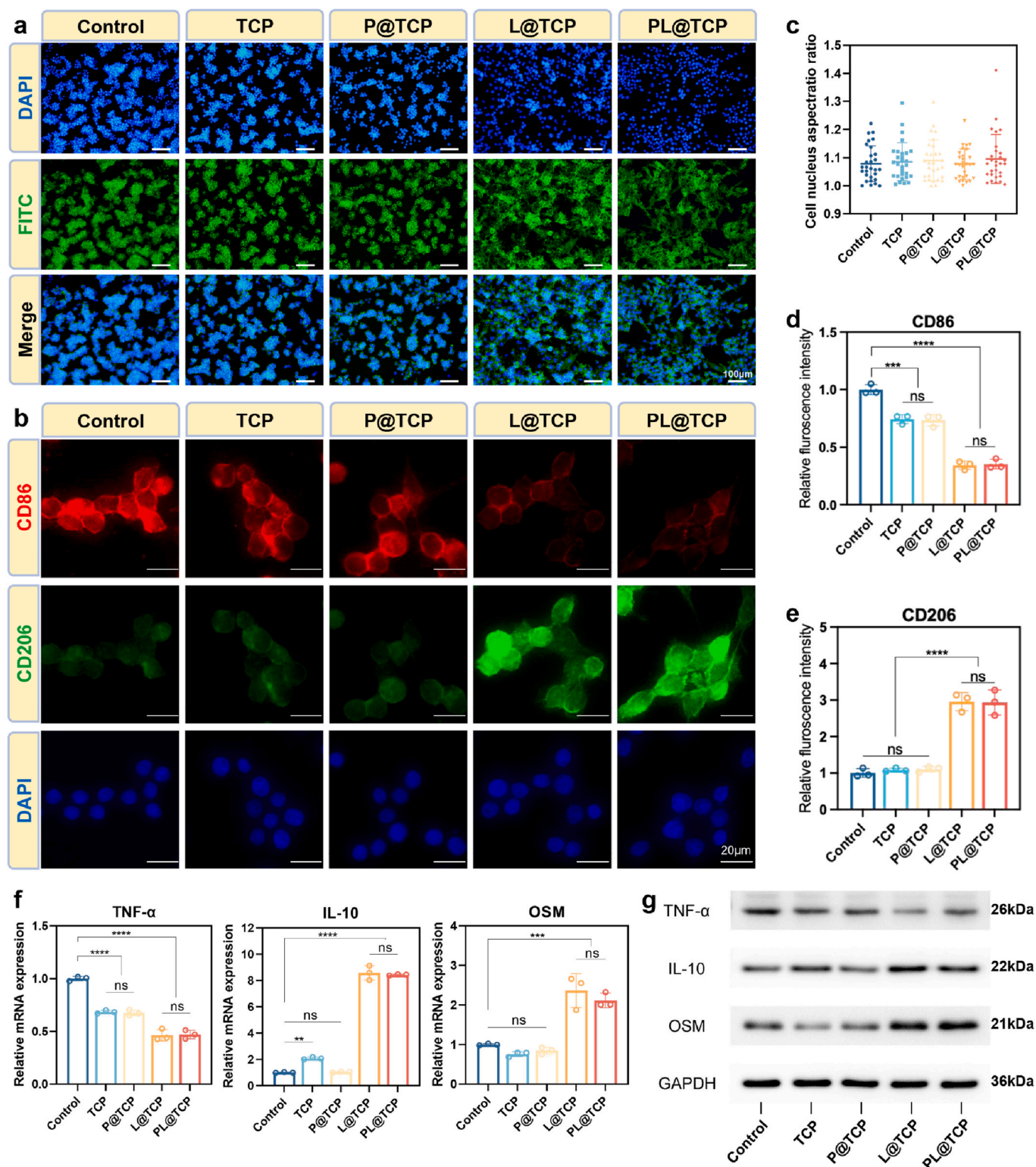
Fig. 4. Immune responses of macrophages cultured on PL@TCP *in vitro*. (a) Nucleus (blue) and cytoskeleton (green) of macrophages on day 3. (b) Immunofluorescent staining of nucleus (blue), CD86 (red) and CD206 (green) of macrophages on day 3. (c) Quantitative cell nucleus aspect ratio based on immunofluorescent images. Quantitative fluorescence intensity of (d) CD86 and (e) CD206 of macrophages. (f) Relative mRNA expression of TNF-α, IL-10 and OSM of macrophages on day 3. (g) Western blot analysis of TNF-α, IL-10 and OSM of macrophages on day 3. **$P < 0.01$, ***$P < 0.001$, ****$P < 0.0001$.

observed that CD86, an important marker of M1 macrophage activation, was located on the cell surface [58]. Additionally, CD206, a highly expressed cell-surface protein on M2 macrophages, was a marker for M2 polarization [59]. Therefore, CD86 and CD206 were chosen for immunofluorescent staining. Fig. 4b shows the results of immunofluorescence staining images and quantified fluorescence intensity. Quantification of nuclear aspect ratio did not show a correlation with the presence or absence of LR or macrophage polarization activation (Fig. 4c). Compared with the control group, L@TCP and PL@TCP showed the most obvious reduction of M1-labeled CD86 (Fig. 4d). Additionally,

L@TCP and PL@TCP had the highest level of CD206, which was significantly higher than the other three groups, indicating that LR could induce M2 macrophage activation (Fig. 4e).

Fig. 4f displays the expression levels of M1 and M2 macrophage-related genes. LR (L@TCP and LP@TCP) exhibited the lowest expression level of M1-related genes (TNF-α) but the highest expression level of M2-related genes (IL-10) compared to non-LR group (control, TCP and P@TCP). Macrophages can also mediate bone regeneration by secreting osteoinductive factors in addition to regulating the inflammatory milieu [60]. For instance, OSM is a powerful inducer of osteogenesis that is secreted by macrophages [36]. Our findings indicate that the trend of OSM expression levels in different samples was similar to that of the M2 macrophage gene (IL-10). The OSM expression levels of L@TCP and LP@TCP were higher than those of the other three groups, while there was no significant difference in the remaining three groups. The post-transcriptional regulation was confirmed through Western-Blot analysis. Fig. 4g shows that L@TCP had the lowest expression of TNF-α and the highest expression of IL-10. PL@TCP was similar to L@TCP, with much lower TNF-α expression than the other groups, much higher IL-10 expression than the other groups, and the highest expression of OSM (Supplementary Fig. 5). PL@TCP appears to inhibit the expression of pro-inflammatory factors and promote the expression of anti-inflammatory factors, thereby activating M2 macrophages. Additionally, high expression of osteoclastogenic cytokines can predictably promote osteogenic differentiation. Thus, this suggests that PL@TCP has the ability to suppress the expression of pro-inflammatory factors and enhance the expression of anti-inflammatory factors, thereby activating M2 macrophages. Additionally, high levels of osteoclastogenic cytokines can predictably stimulate osteogenic differentiation.

3.5. Effects of immune microenvironment of PL@TCP on osteogenesis of BMSCs

3.5.1. Macrophage cytokines modulate osteogenic differentiation of BMSCs in vitro

Osteomyelitis can cause bone destruction. The implant used for treatment should have excellent properties to promote osteogenesis to avoid implant failure and the risk of multiple surgeries and bone nonunion. To investigate the effect of PL@TCP-induced macrophage polarization on the osteogenic differentiation of BMSCs, RAW 264.7 macrophages were seeded on different scaffolds for 72 h. The collected supernatants of macrophages (CM) were incubated with BMSCs. It is known that a higher number of BMSCs result in a better osteogenic effect. After 48 h, cytoskeletal staining with FITC revealed distinct morphology and increased attachment of BMSCs (Fig. 5a). The BMSCs in the CM^L@TCP and CM^PL@TCP groups exhibited linear pseudopod polygons, while those in the other three groups appeared fusiform in shape. The increased number of attachments and the change in BMSCs morphology suggest that LR-activated macrophages can promote in vitro osteogenesis, which is a prerequisite for bone repair. To assess early osteogenic differentiation, alkaline phosphatase (ALP) staining was performed on BMSCs cultures after 3 and 7 days. Blue ALP indicated better differentiation in CM^L@TCP and CM^PL@TCP (Fig. 5b). Calcium deposition was assessed using Alizarin red staining at 14 and 21 days.
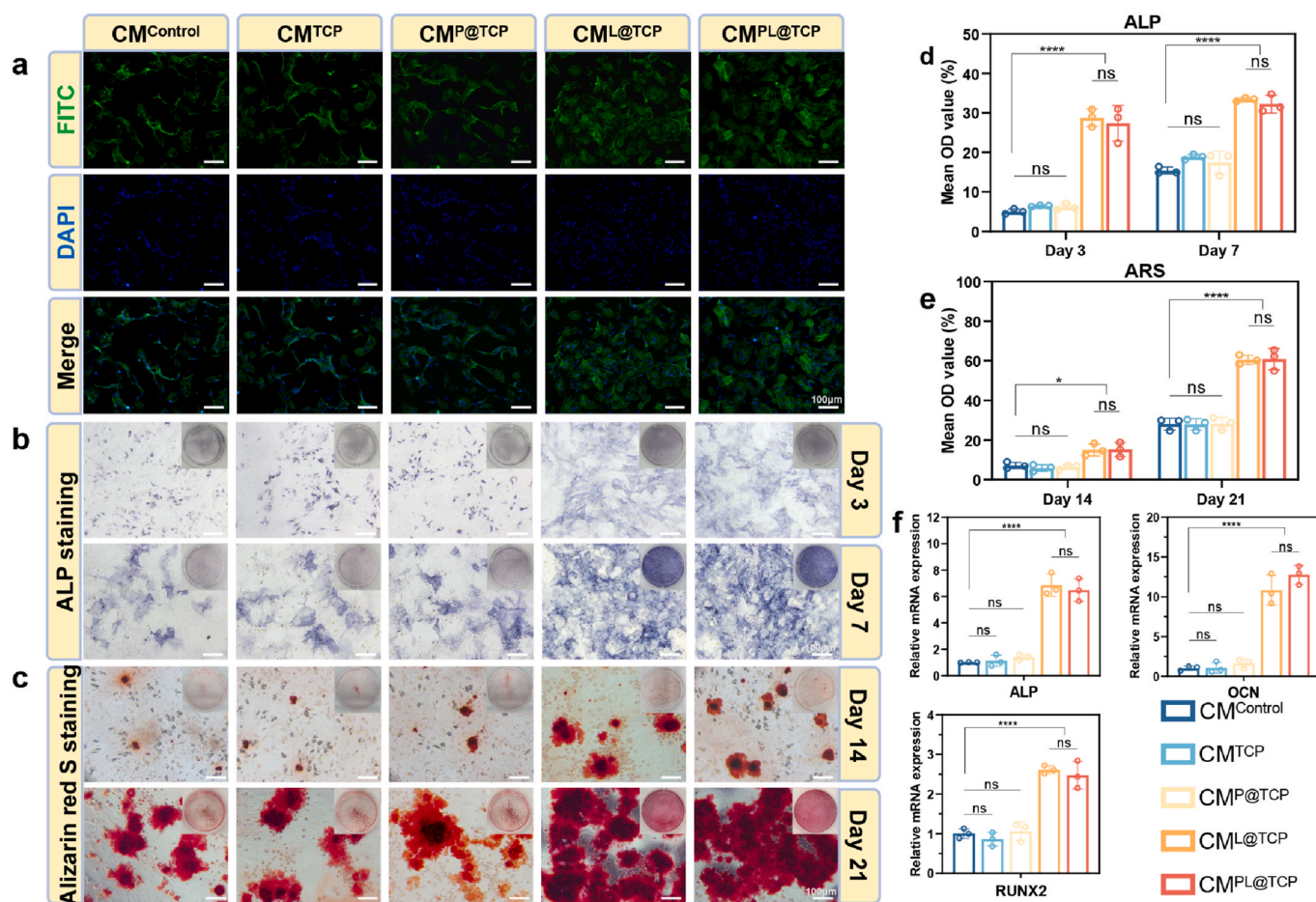

Fig. 5. Osteogenic differentiation of BMSCs cultured with macrophage cytokines collected from PL@TCP *in vitro*. (a) Nucleus (blue) and cytoskeleton (green) of BMSCs on day 2. (b) ALP staining of BMSCs on day 3 and 7. (c) Alizarin Red S staining of BMSCs on day 14 and 21. Quantitative analysis of (d) ALP staining and (e) Alizarin Red S staining. (f) Relative mRNA expression of ALP, RUNX2 and OCN of BMSCs on day 7. *P < 0.05, ****P < 0.0001.

Fig. 5c shows that CM$^{L@TCP}$ and CM$^{PL@TCP}$ induce the highest matrix mineralization. ALP and mineral deposition were quantified using ImageJ software. Fig. 5(d and e) shows that the OD values of CM$^{L@TCP}$ and CM$^{PL@TCP}$ were higher than the other three groups. Osteogenesis-related gene expression of ALP, RUNX2, and OCN were detected on day 7. The RT-PCR results in Fig. 5f show significant high expression of ALP, RUNX2, and OCN in CM$^{L@TCP}$ and CM$^{PL@TCP}$. Based on these results, PL@TCP exhibits better biocompatibility and significant *in vitro* stimulation of bone regeneration properties. The host immune response plays a critical role in osteointegration [38]. These results suggest that PL@TCP-induced M2 macrophages secrete cytokines IL-10 and OSM, which, in turn, promote osteogenic differentiation of BMSCs.

3.5.2. PL@TCP directly promoted osteogenic differentiation in vitro

To validate the direct osteogenic properties of this sample, we simulated the microenvironment after implantation into the host. PL@TCP was cultured with BMSCs, and macrophage supernatants were added to the culture. After 48 h, live-dead cell staining showed no significant cytotoxicity of PL@TCP (Fig. 6a). On day 7, ALP staining revealed a darker and denser distribution of blue ALP when PL@TCP was coupled with cytokines stimulated by macrophages. This was observed both with the naked eye and under a microscope at $100\times$ magnification (Fig. 6b). On day 21, PL@TCP + CM$^{PL@TCP}$ exhibited the best mineral deposition (Fig. 6c), as evidenced by a higher OD value compared to the other two groups, as shown in Fig. 6(d and e). It is evident that using PL@TCP alone has a superior osteogenic effect. Additionally, macrophage activation contributes to a favorable immune microenvironment that promotes osseointegration. This supports the implant's need to achieve both osteogenic differentiation and simultaneous immune cell activation to enhance the osteogenic effect when introduced into the host.

3.6. PL@TCP promotes antimicrobial and osseointegration in vivo

In vitro studies have demonstrated the potential of PL@TCP for antimicrobial and osteogenic applications. Specifically, P@TCP exhibited a more comprehensive antimicrobial profile, while L@TCP showed advantages in osteogenesis. Therefore, an infection defect model was used to evaluate the combined antimicrobial and osteogenic properties of the PL@TCP, P@TCP, and L@TCP scaffolds. Osteomyelitis with *S. aureus* infection is more common than *E.coli* infection in the clinic, therefore, we modeled cranial osteomyelitis in the context of *S. aureus* infection (Fig. 7a) [61]. An infected cranial defect by filling gelatin sponges with *S.aureus* to simulate osteomyelitis. Two weeks after bacterial implantation, the skull was re-exposed through the same midline scalp wound. Micro CT imaging revealed sinus tracts around the bone defect (Supplementary Fig. 6). The resulting defect was filled with biomaterial after removal of infected tissue. At week 2 post-surgery, the general photographs showed that groups without phage (Control, TCP, L@TCP) showed more severe blood accumulation and swelling (Supplementary Fig. 7). As the phage eliminated the infection, the P@TCP and PL@TCP groups had cleaner skull surfaces and fewer haematomas. The rats were euthanized at 4 and 8 weeks postoperatively, and the bone defect area was collected for follow-up examination. We used plate counting methods to assess the therapeutic efficacy of PL@TCP in eliminating *S. aureus* from cranial bone samples, utilizing bone marrow tissue harvested at week 4 postoperatively. The results showed minimal colony formation with P@TCP and PL@TCP, indicating
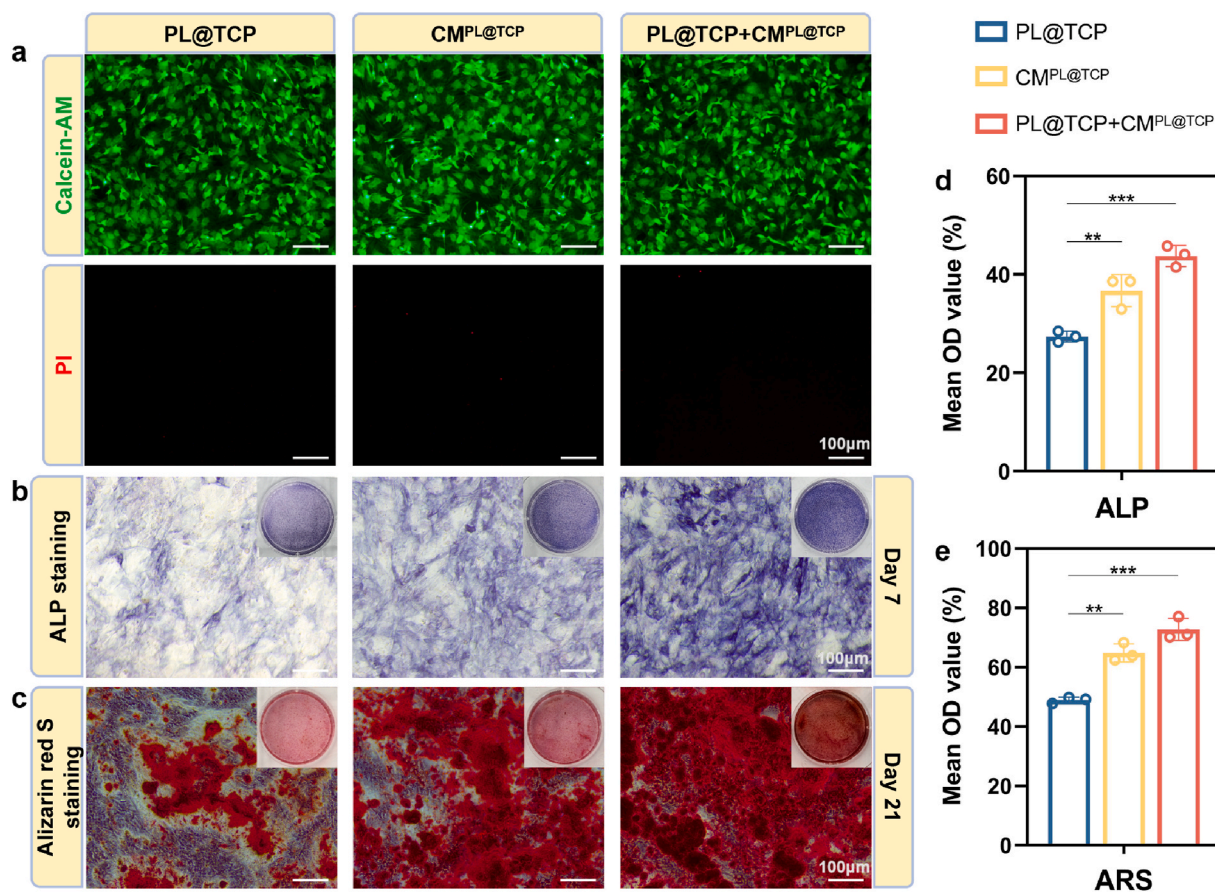

Fig. 6. Osteogenic differentiation of BMSCs cultured on PL@TCP with macrophage cytokines collected from PL@TCP *in vitro*. (a) Live (green)/dead (red) staining of BMSCs on day 2. (b) ALP staining of BMSCs on day 7. (c) Alizarin Red S staining of BMSCs on day 21. Quantitative analysis of (d) ALP staining and (e) Alizarin Red S staining. **$P < 0.01$, ***$P < 0.001$.
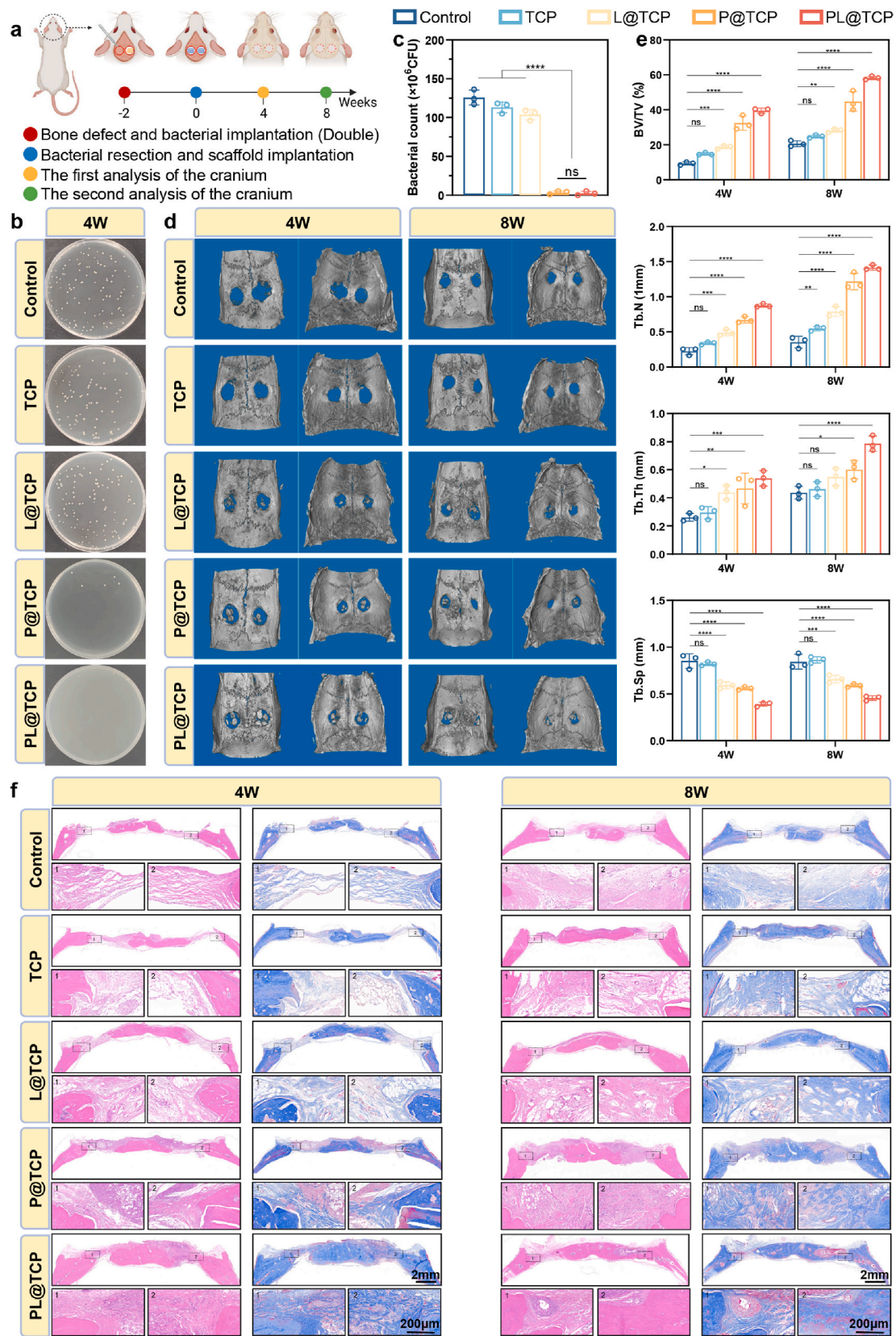
Fig. 7. Antimicrobial and osteogenic properties of PL@TCP *in vivo*. (a) Scheme presented the process of osteomyelitis model establishment, bacterial resection, scaffold implantation, antimicrobial and osteogenic analysis. (b) Antibacterial effects on *S. aureus* at week 4 post-surgery. (c) Quantitative analysis of bacterial colonies of *S. aureus*. (d) 3D micro-CT images of cranium at week 4 and 8 post-surgery. (e) Quantitative analysis of osteogenesis-related parameters including BV/TV, Tb.N, Tb.Th and Tb.Sp. (f) H&E staining and Masson staining for bone defects and surrounding normal bones at week 4 and 8 post-surgery. *P < 0.05, **P < 0.01, ***P < 0.001, ****P < 0.0001.

the potential therapeutic efficacy of PL@TCP in *S.aureus*-infected osteomyelitis (Fig. 7b and c). As illustrated in the Giemsa staining at week 4, the numbers of bacteria declined significantly in the PL@TCP compared with Control (Supplementary Fig. 8). Using Micro-CT, we observed bone regeneration through three-dimensional reconstruction of consecutive scanned images. At week 4, abnormal borders were observed within the infected bones in the Control and TCP groups, as well as bone erosion resembling insect bites, which surrounded the infected bones described above, with almost no visible new bone (Fig. 7d). In the L@TCP group, bone erosion and sinusoids were observed, but some osteogenesis was present. In contrast, bacteria that scavenge phages and were implanted in P@TCP and PL@TCP did not show any signs of infection. Compared to other treatments, PL@TCP exhibited more inward growth of bone tissue from the edge of the bone defect to the interior, facilitating the repair of large bone defects. At week 8, PL@TCP demonstrated the highest level of osseointegration. L@TCP and P@TCP exhibited lower levels of osseointegration, while the control group and TCP alone showed the least. Additionally, we conducted a bone parameter analysis to verify the formation of new bone tissue. Micro-CT-generated bone parameters, such as bone volume/tissue volume (BV/TV), trabecular number (Tb.N), trabecular thickness (Tb.Th), and trabecular spacing (Tb.Sp), demonstrated that the PL@TCP scaffold is ideal for stimulating bone regeneration *in vivo* (Fig. 7e).

H&E and Masson staining revealed large stained areas, indicating greater bone tissue formation in the PL@TCP scaffolds. The scaffold's three-dimensional structure provided support, facilitating cell and tissue growth, and communication within the interlaced pore structure, provided the infection was cleared (Fig. 7f). The immunofluorescence staining results of macrophages showed higher levels of CD206 expression and lower levels of CD86 expression in the PL@TCP group (Fig. 8a and b). Statistical analysis indicated that macrophages tended to polarize towards M2 after implantation of the scaffold, which was consistent with the results of *in vitro* experiments (Fig. 8c and d). Additionally, OCN and osteopontin (OPN) are proteins expressed at the end of osteoblast differentiation. Bone tissue growth was verified through immunofluorescence staining that detected OCN and OPN in the bone (Fig. 8d). The PL@TCP scaffold accelerated bone regeneration, and its osteogenic capacity of the scaffolds was characterized at the protein level through immunohistochemical analysis (Fig. 8e and f).

During the bone regeneration stage, higher levels of RUNX2, BMP-2, and CD146 proteins were expressed in the PL@TCP group (Fig. 8g and Supplementary Fig. 9). To determine if the samples caused any systemic side effects, we performed H&E staining on the major organs of rats treated with the samples. No significant tissue toxicity was observed (Supplementary Fig. 10). Evidence suggests that PL@TCP can be implanted into the bone defect area after osteomyelitis debridement to achieve both anti-infection and bone repair.

3.7. Transcriptome analysis reveals how PL@TCP acts on macrophages and BMSCs

3.7.1. Transcriptomic analysis shows PL@TCP-induced macrophage polarization pathways

To understand how PL@TCP activates macrophage polarization, we performed transcriptomic analysis on PL@TCP and unmodified TCP-cultured macrophages. We first assessed the stability of the samples by conducting a Pearson correlation analysis between them. The majority of the correlation coefficients were within an acceptable range ($R^2 > 0.95$) (Fig. 9a). As shown in Fig. 9b, the volcano plot displays 453 up-regulated genes and 253 down-regulated genes, indicating a significant degree of differential gene expression. The differentially expressed genes were analyzed using the gene ontology (GO) database, where they were typically categorized into three categories: biological process (BP), molecular function (MF), and cellular component (CC). Fig. 9c displayed the top 20 enriched terms that were up-regulated for PL@TCP over TCP. The enrichment of genes coding for cytokines that regulate cell adhesion was associated with changes in macrophage morphology caused by LR biofilm on the surface of PL@TCP. To analyze potential signaling pathways, we performed Kyoto Encyclopedia of Genes and Genomes (KEGG). The top-enriched up-KEGG pathway was shown in Fig. 9d (the words in red), which revealed an upregulation of the extracellular matrix (ECM) receptor interaction signaling pathway. This pathway had been shown to be associated with M2 macrophage activation and bone regeneration [62,63]. The ECM is a complex mixture of structural and functional macromolecules that plays a crucial role in tissue and organ morphogenesis, as well as in the maintenance of cell and tissue structure and function. In contrast, the pathways associated with the activation of M1 macrophages, such as IL-17 [64], TNF [65], and NF-κB(nuclear
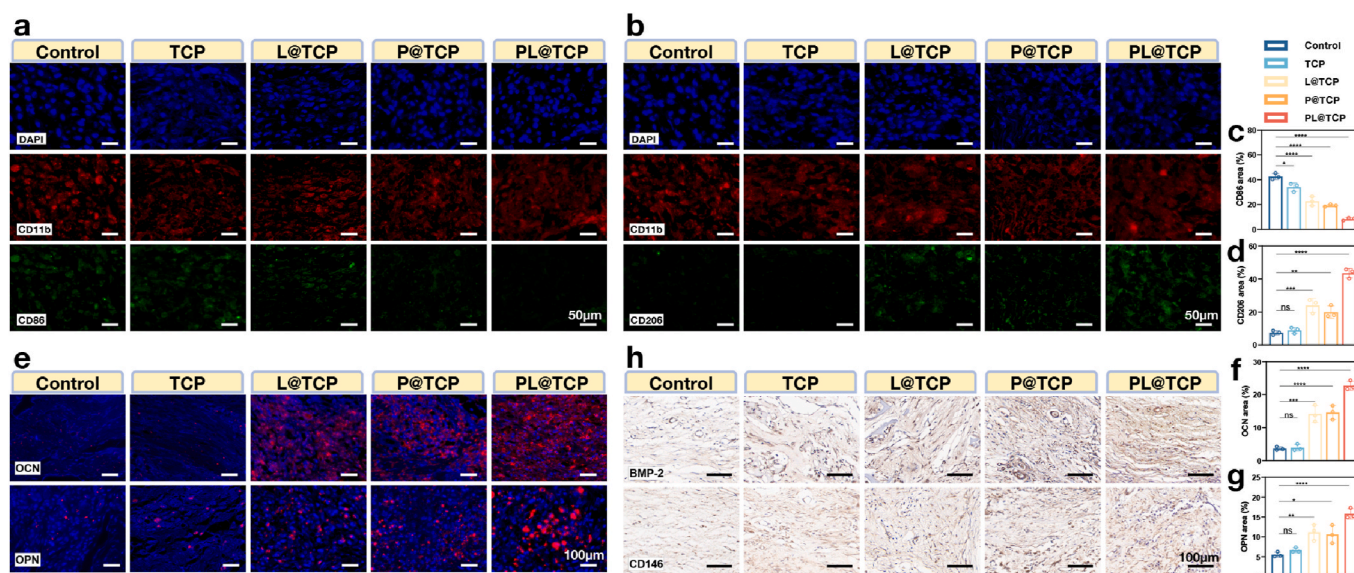

Fig. 8. M2 polarizating and osteogenic properties of PL@TCP *in vivo*. Immunofluorescent staining of nucleus, CD11b, (a) CD86 and (b) CD206 in defect areas at week 4 post-surgery. Quantitative fluorescence intensity of (c) CD86 and (d) CD206 based on immunofluorescent images. (e) Immunohistochemical staining of OCN and OPN in defect areas at week 4 post-surgery. Quantitative fluorescence intensity of (f) OCN and (g) OPN. (h) Immunohistochemical staining of BMP-2 and CD146 in defect areas at week 4 post-surgery. *$P < 0.05$, **$P < 0.01$, ***$P < 0.001$, ****$P < 0.0001$.
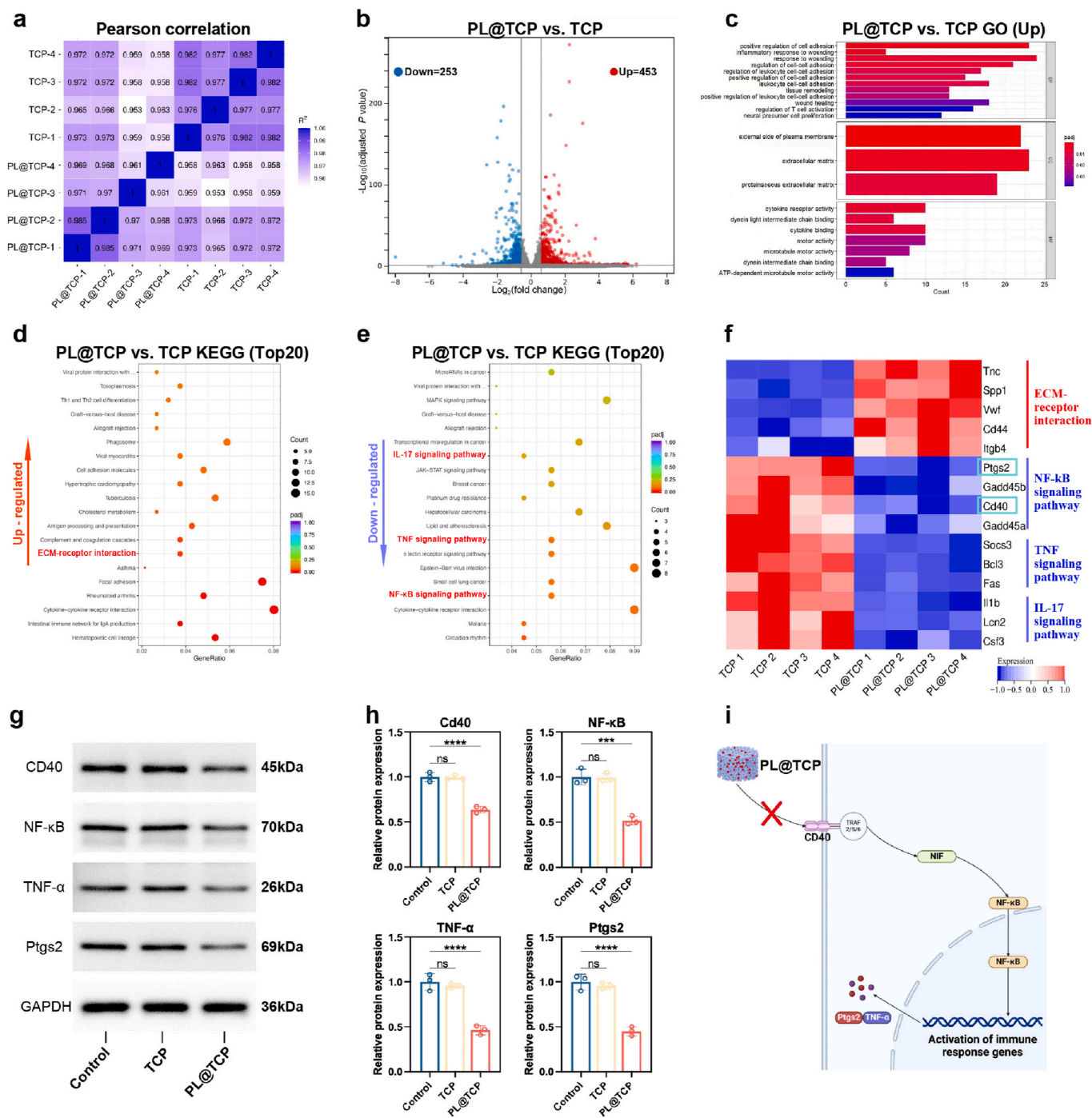
Fig. 9. Bioinformatic analysis of macrophage gene expression on PL@TCP. (a) Heatmap of Pearson correlation between samples. (b) Volcano plot of transcriptomic analysis of differentially expressed genes. (c) Up-regurated GO analysis of all genes in macrophages cultured on PL@TCP versus TCP. (d) Up-regurated and (e) down-regulated KEGG enrichment pathways of PL@TCP versus TCP. (f) Heatmap of differentially expressed genes of ECM-receptor interaction, NF-κB, TNF and IL-17 signaling pathway. (g) Western blot analysis of CD40, NF-κB, TNF-α and Ptgs2 of macrophages and (h) quantitative analysis of protein expression based on Western blot images. (I) Schematic diagram of PL@TCP inhibiting NF-κB signaling pathway. ***$P < 0.001$, ****$P < 0.0001$.

factor κ light chain enhancer of activated B cells) [66], were down-regulated after PL@TCP treatment (the words in red, Fig. 9e). Further analysis of the normalized heatmap revealed a significant down-regulation in the expression of genes associated with inflammation and relative chemotactic factors following PL@TCP treatment (Fig. 9f). ECM receptor interaction pathway genes were significantly up-regulated in PL@TCP compared to TCP. The presence of Ptgs2 and CD40 in heatmap provided insight into the mechanism of the NF-κB pathway. It was established that the NF-κB signaling pathway played a

crucial role in mediating inflammatory responses [67]. CD40 is a member of the tumour necrosis factor receptor superfamily, which functions as an upstream regulator of the NF-κB pathway and is primarily responsible for the differentiation of macrophages into the M1-type [68]. CD40 promotes the synthesis of NF-κB through the activation of NIK (NF-κB-inducing kinase), which enters the nucleus of the cell and initiates the synthesis of immune-responsive genes, which in turn promotes the downstream synthesis of inflammatory factors, such as TNF-α and Ptgs2 (Cox2) [69,70]. The Western blot experiment

revealed a reduction in the intensity of the bands corresponding to CD40, NF-κB, TNF-α and Ptgs2 in the PL@TCP group compared to Control and TCP groups (Fig. 9g). Subsequent statistical analysis revealed a notable decline in the levels of CD40, NF-κB, TNF-α and Ptgs2 following PL@TCP treatment (Fig. 9h). These findings indicated that PL@TCP had a notable anti-inflammatory effect through inhibiting NF-κB signaling pathway (Fig. 9i).

3.7.2. Transcriptomic analysis of PL@TCP promotes the osteogenic differentiation in BMSCs

To explore how PL@TCP enhances osteogenic differentiation in BMSCs, we used transcriptomic analysis on PL@TCP and unmodified TCP-cultured BMSCs. Pearson correlation analysis demonstrated that the majority of the correlation coefficients were within an acceptable range ($R2 > 0.90$) (Fig. 10a). The total number of differentially expressed genes was 3330, including 1790 upregulated genes and 1540 downregulated genes in PL@TCP versus TCP (Fig. 10b), indicating a significant difference in gene expression. KEGG analysis was performed

to reveal the key osteogenic signaling pathways. Among the top 20 up-regulated pathways, four were related to osteogenesis (the words in red, Fig. 10c). Further analysis of the normalized heatmap revealed a significant up-regulation in the expression of genes associated with ECM-receptor interaction, Calcium signaling pathway, Wnt signaling pathway and TGF-beta signaling pathway following PL@TCP treatment (Fig. 10d). It is reported that ECM-receptor interaction enhances extracellular mechanisms and promotes osteoblast proliferation, providing a favorable environment for bone formation [71]. Furthermore, Ca-ions are core components of bone tissue and up-regulation of the calcium signaling pathway promotes Ca-ion deposition in bone [72]. The Wnt pathway maintains stem cell function and increases bone matrix deposition [73]. TGF-beta signaling pathway promotes osteoblast differentiation and chondrocyte differentiation, which are key to osteogenesis [74]. An insight into the mechanism of the TGF-beta pathway was provided by the presence of Bmp2 and Smad9 in the heatmap. As known, Bmp2 activates the intracellular TGF-beta signaling pathway by binding to receptors on the surface of the cell membrane [75]. Smad is a
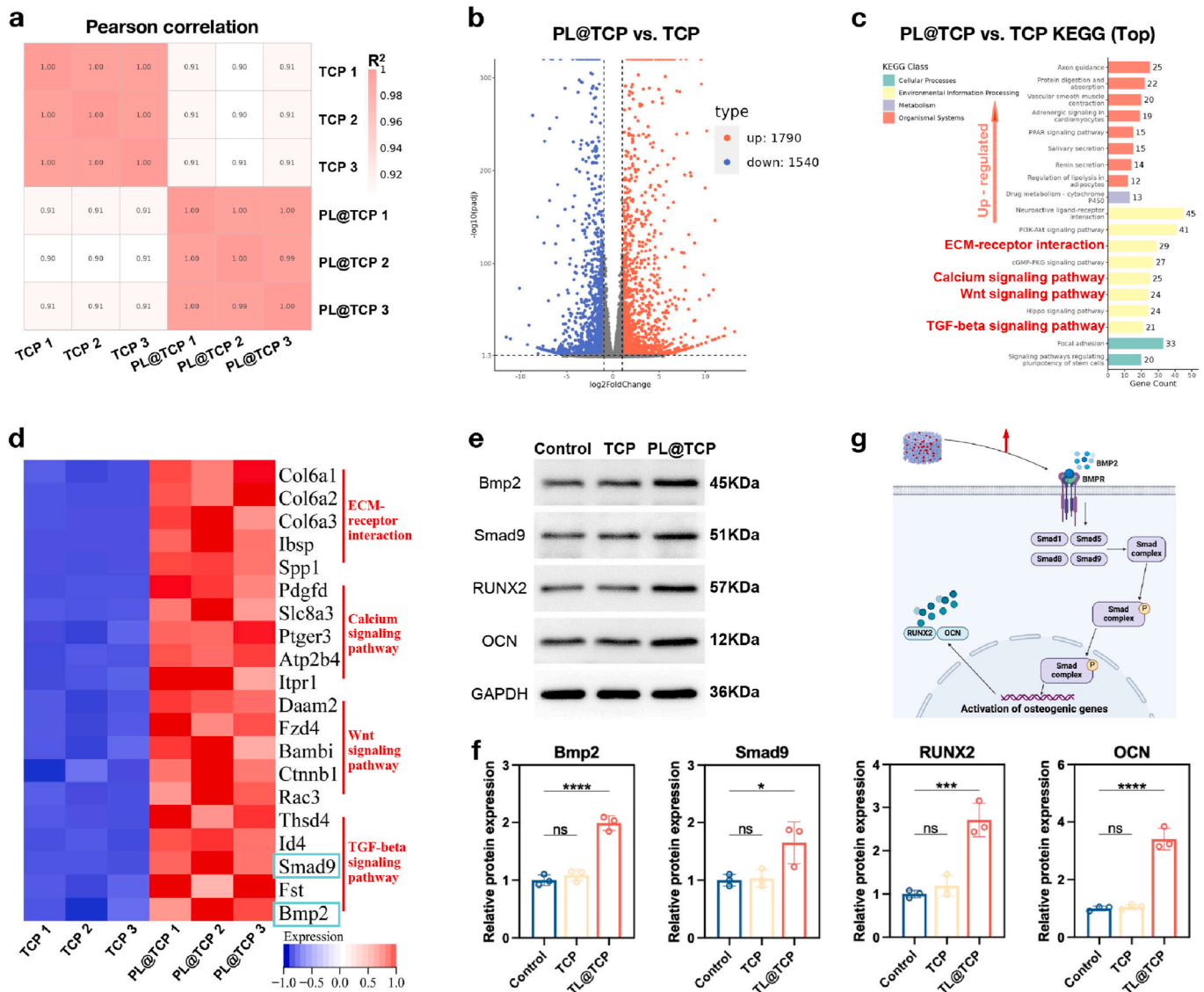

Fig. 10. Bioinformatic analysis of BMSC gene expression on PL@TCP. (a) Heatmap of Pearson correlation between samples. (b) Volcano plot of transcriptomic analysis of differentially expressed genes. (c) Up-regurated KEGG enrichment pathways of PL@TCP versus TCP. (d) Heatmap of differentially expressed genes of ECM-receptor interaction, Calcium, Wnt and TGF-beta signaling pathway. (e) Western blot analysis of Bmp2, Smad9, RUNX2 and OCN2 of BMSCs and (f) quantitative analysis of protein expression based on Western blot images. (g) Schematic diagram of PL@TCP enhancing TGF-beta signaling pathway. $*P < 0.5$, $***P < 0.001$, $****P < 0.0001$.

key signaling molecule in the TGF-beta signaling pathway [76]. Smad9 is one of the components that make up the Smad complex. Following phosphorylation of the Smad complex, it enters the nucleus of the cell and activates the expression of genes involved in osteogenesis, such as RUNX2 and OCN2, thereby inducing osteogenic differentiation of BMSCs [77]. The Western blot experiment showed a notable increase in the intensity of the bands corresponding to Bmp2, Smad9, RUNX2 and OCN2 in the PL@TCP group compared to Control and TCP group (Fig. 10e). Further statistical analysis revealed a significant enhancement in the levels of Bmp2, Smad9, RUNX2 and OCN2 following PL@TCP treatment (Fig. 10f). In brief, gene and protein expression of TGF-beta signaling pathways demonstrated a significant osteogenic effect after modification of LR biofilm on TCP (Fig. 10g).

4. Conclusion

This study rationalized the use of phage and probiotic biofilm-modified TCPs for constructing bioactive implants and demonstrated their potential in treating osteomyelitis. Conventional implants are not bioactive and often carry drugs that have difficulty penetrating the biofilm barrier in osteomyelitis, leading to treatment failure. We utilized the property that phages can lyse the corresponding bacterial biofilm to eliminate *E. coli* and *S. aureus* infections. LR-coated implants maintained immune cell activation despite inactivation. Probiotic biofilms demonstrated an immunomodulatory effect that reduced inflammation and increased the expression of anti-inflammatory factors. PL@TCP promoted macrophage polarization towards the M2 type by reducing the classical pro-inflammatory pathway (NF-κB signaling pathway). Additionally, it promoted bone growth in defects caused by osteomyelitis, offering additional therapeutic benefits to address bone damage following infection. PL@TCP enhanced osteogenic differentiation of BMSC, with the upregulation of the key osteogenic pathway (TGF-beta signaling pathway). Promising therapeutic results were observed in a rat model of osteomyelitis. In conclusion, we presented a promising anti-infective and bone-enabling approach to design bioactive implants that bridged the gap between many traditional implants in the management of osteomyelitis.

CRediT authorship contribution statement

Junwei Su: Writing – review & editing, Writing – original draft, Methodology, Investigation, Data curation, Conceptualization. **Yifan Wu:** Writing – review & editing, Software, Resources, Formal analysis, Data curation. **Zheng Wang:** Writing – review & editing, Visualization, Methodology, Formal analysis. **Dong Zhang:** Writing – review & editing, Visualization, Validation, Software. **Xianquan Yang:** Writing – review & editing, Validation, Funding acquisition, Formal analysis. **Yong Zhao:** Writing – review & editing, Validation, Software, Methodology, Investigation, Funding acquisition, Conceptualization. **Aixi Yu:** Writing – review & editing, Supervision, Resources, Project administration, Investigation, Funding acquisition, Conceptualization.

Declaration of competing interest

The authors declare that they have no known competing financial interests or personal relationships that could have appeared to influence the work reported in this paper.

Appendix B. Supplementary data

Supplementary data to this article can be found online at https://doi.org/10.1016/j.mtbio.2025.101444.

Data availability

Data will be made available on request.

References

[1] C. Zhong, Y. Wu, H. Lin, R. Liu, Advances in the antimicrobial treatment of osteomyelitis, Compos. B Eng. 249 (2023) 110428, https://doi.org/10.1016/j.compositesb.2022.110428.

[2] N. Kavanagh, E.J. Ryan, A. Widaa, G. Sexton, J. Fennell, S. O'Rourke, K.C. Cahill, C.J. Kearney, F.J. O'Brien, S.W. Kerrigan, Staphylococcal osteomyelitis: disease progression, treatment challenges, and future directions, Clin. Microbiol. Rev. 31 (2018), https://doi.org/10.1128/cmr.00084-17, 10.1128/cmr.00084-17.

[3] M. Dudareva, A.J. Hotchen, J. Ferguson, S. Hodgson, M. Scarborough, B.L. Atkins, M.A. McNally, The microbiology of chronic osteomyelitis: changes over ten years, J. Infect. 79 (2019) 189–198, https://doi.org/10.1016/j.jinf.2019.07.006.

[4] X. Wang, M. Zhang, T. Zhu, Q. Wei, G. Liu, J. Ding, Flourishing antibacterial strategies for osteomyelitis therapy, Adv. Sci. 10 (2023) 2206154, https://doi.org/10.1002/advs.202206154.

[5] R.A. Drummond, J.V. Desai, E.E. Ricotta, M. Swamydas, C. Deming, S. Conlan, M. Quinones, V. Matei-Rascu, L. Sherif, D. Lecky, C.-C.R. Lee, N.M. Green, N. Collins, A.M. Zelazny, D.R. Prevots, D. Bending, D. Withers, Y. Belkaid, J. A. Segre, M.S. Lionakis, Long-term antibiotic exposure promotes mortality after systemic fungal infection by driving lymphocyte dysfunction and systemic escape of commensal bacteria, Cell Host Microbe 30 (2022) 1020–1033.e6, https://doi.org/10.1016/j.chom.2022.04.013.

[6] C. de la Fuente-Nunez, A. Cesaro, R.E.W. Hancock, Antibiotic failure: beyond antimicrobial resistance, Drug Resist. Updates 71 (2023) 101012, https://doi.org/10.1016/j.drup.2023.101012.

[7] C.R. MacNair, S.T. Rutherford, M.-W. Tan, Alternative therapeutic strategies to treat antibiotic-resistant pathogens, Nat. Rev. Microbiol. (2023), https://doi.org/10.1038/s41579-023-00993-0.

[8] S. McCallin, Z. Drulis-Kawa, T. Ferry, J.-P. Pirnay, R. Nir-Paz, Phages and phage-borne enzymes as new antibacterial agents, Clin. Microbiol. Infection (2023), https://doi.org/10.1016/j.cmi.2023.10.018.

[9] R.Y.K. Chang, S.C. Nang, H.-K. Chan, J. Li, Novel antimicrobial agents for combating antibiotic-resistant bacteria, Adv. Drug Deliv. Rev. 187 (2022) 114378, https://doi.org/10.1016/j.addr.2022.114378.

[10] D. Liu, J.D. Van Belleghem, C.R. de Vries, E. Burgener, Q. Chen, R. Manasherob, J. R. Aronson, D.F. Amanatullah, P.D. Tamma, G.A. Suh, The safety and toxicity of phage therapy: a review of animal and clinical studies, Viruses 13 (2021) 1268, https://doi.org/10.3390/v13071268.

[11] A.L. Clarke, S. De Soir, J.D. Jones, The safety and efficacy of phage therapy for bone and joint infections: a systematic review, Antibiotics (Basel) 9 (2020) 795, https://doi.org/10.3390/antibiotics9110795.

[12] M. Żaczek, A. Górski, B. Weber-Dąbrowska, S. Letkiewicz, W. Fortuna, P. Rogóż, E. Pasternak, R. Międzybrodzki, A thorough synthesis of phage therapy unit activity in Poland—its history, milestones and international recognition, Viruses 14 (2022) 1170, https://doi.org/10.3390/v14061170.

[13] G.M. de F. Almeida, L.-R. Sundberg, The forgotten tale of Brazilian phage therapy, Lancet Infect. Dis. 20 (2020) e90–e101, https://doi.org/10.1016/S1473-3099(20)30060-8.

[14] F.L. Gordillo Altamirano, J.J. Barr, Phage therapy in the postantibiotic era, Clin. Microbiol. Rev. 32 (2019), https://doi.org/10.1128/CMR.00066-18, 00066-18.

[15] C. Schwarz, J. Mathieu, J.A. Laverde Gomez, P. Yu, P.J.J. Alvarez, Renaissance for phage-based bacterial control, Environ. Sci. Technol. 56 (2022) 4691–4701, https://doi.org/10.1021/acs.est.1c06232.

[16] S. Hesse, S. Adhya, Phage therapy in the twenty-first century: facing the decline of the antibiotic era; is it finally time for the age of the phage? Annu. Rev. Microbiol. 73 (2019) 155–174, https://doi.org/10.1146/annurev-micro-090817-062535.

[17] G.A. Suh, T. Ferry, M.P. Abdel, Phage therapy as a novel therapeutic for the treatment of bone and joint infections, Clin. Infect. Dis. 77 (2023) S407–S415, https://doi.org/10.1093/cid/ciad533.

[18] J. Young, S.W. Lee, M.J. Shariyate, A. Cronin, J.J. Wixted, A. Nazarian, C. F. Rowley, E.K. Rodriguez, Bacteriophage therapy and current delivery strategies for orthopedic infections: a SCOPING review, J. Infect. 88 (2024) 106125, https://doi.org/10.1016/j.jinf.2024.106125.

[19] P.J. Simner, J. Cherian, G.A. Suh, Y. Bergman, S. Beisken, J. Fackler, M. Lee, R. J. Hopkins, P.D. Tamma, Combination of phage therapy and cefiderocol to successfully treat Pseudomonas aeruginosa cranial osteomyelitis, JAC-Antimicrobial Resistance 4 (2022), https://doi.org/10.1093/jacamr/dlac046 dlac046.

[20] M.J. Young, L.M.L. Hall, M. Merabishvilli, J.-P. Pirnay, J.R. Clark, J.D. Jones, Phage therapy for diabetic foot infection: a case series, Clin. Therapeut. 45 (2023) 797–801, https://doi.org/10.1016/j.clinthera.2023.06.009.

[21] J.B. Doub, A.J. Johnson, S. Nandi, V. Ng, T. Manson, M. Lee, B. Chan, Experience using adjuvant bacteriophage therapy for the treatment of 10 recalcitrant

periprosthetic joint infections: a case series, Clin. Infect. Dis. 76 (2023) e1463–e1466, https://doi.org/10.1093/cid/ciac694.

[22] C. Zhao, W. Liu, M. Zhu, C. Wu, Y. Zhu, Bioceramic-based scaffolds with antibacterial function for bone tissue engineering: a review, Bioact. Mater. 18 (2022) 383–398, https://doi.org/10.1016/j.bioactmat.2022.02.010.

[23] L. Tan, J. Li, X. Liu, Z. Cui, X. Yang, S. Zhu, Z. Li, X. Yuan, Y. Zheng, K.W.K. Yeung, H. Pan, X. Wang, S. Wu, Rapid biofilm eradication on bone implants using red phosphorus and near-infrared light, Adv. Mater. 30 (2018) 1801808, https://doi.org/10.1002/adma.201801808.

[24] G. Chu, M. Guan, J. Jin, Y. Luo, Z. Luo, T. Shi, T. Liu, C. Zhang, Y. Wang, Mechanochemically reprogrammed interface orchestrates neutrophil bactericidal activity and apoptosis for preventing implant-associated infection, Adv. Mater. (2024) 2311855, https://doi.org/10.1002/adma.202311855.

[25] Y. Hong, H. Fan, B. Li, B.Guo, M. Liu, X. Zhang, Fabrication, biological effects, and medical applications of calcium phosphate nanoceramics, Mater. Sci. Eng. R Rep. 70 (2010) 225–242, https://doi.org/10.1016/j.mser.2010.06.010.

[26] E. Meurice, E. Rguiti, A. Brutel, J.-C. Hornez, A. Leriche, M. Descamps, F. Bouchart, New antibacterial microporous CaP materials loaded with phages for prophylactic treatment in bone surgery, J. Mater. Sci. Med. 23 (2012) 2445–2452, https://doi.org/10.1007/s10856-012-4711-6.

[27] M. Han, W. Lei, J. Liang, H. Li, M. Hou, Z. Gao, The single-cell modification strategies for probiotics delivery in inflammatory bowel disease: a review, Carbohydr. Polym. 324 (2024) 121472, https://doi.org/10.1016/j.carbpol.2023.121472.

[28] W.F. Van Zyl, S.M. Deane, L.M.T. Dicks, Molecular insights into probiotic mechanisms of action employed against intestinal pathogenic bacteria, Gut Microb. 12 (2020) 1831339, https://doi.org/10.1080/19490976.2020.1831339.

[29] F. Wang, M. Song, X. Lu, X. Zhu, J. Deng, Gut microbes in gastrointestinal cancers, Semin. Cancer Biol. 86 (2022) 967–975, https://doi.org/10.1016/j.semcancer.2021.03.037.

[30] C. Li, Z. Wang, H. Xiao, F. Wu, Intestinal delivery of probiotics: materials, strategies, and applications, Adv. Mater. (2024) 2310174, https://doi.org/10.1002/adma.202310174.

[31] J. Walter, R.A. Britton, S. Roos, Host-microbial symbiosis in the vertebrate gastrointestinal tract and the Lactobacillus reuteri paradigm, Proc. Natl. Acad. Sci. U. S. A. 108 (Suppl 1) (2011) 4645–4652, https://doi.org/10.1073/pnas.1000099107.

[32] J.D. Schepper, F.L. Collins, N.D. Rios-Arce, S. Raehtz, L. Schaefer, J.D. Gardinier, R. A. Britton, N. Parameswaran, L.R. McCabe, Probiotic Lactobacillus reuteri prevents postantibiotic bone loss by reducing intestinal dysbiosis and preventing barrier disruption, J. Bone Miner. Res. 34 (2019) 681–698, https://doi.org/10.1002/jbmr.3635.

[33] J.D. Schepper, F. Collins, N.D. Rios-Arce, H.J. Kang, L. Schaefer, J.D. Gardinier, R. Raghuvanshi, R.A. Quinn, R. Britton, N. Parameswaran, L.R. McCabe, Involvement of the gut microbiota and barrier function in glucocorticoid-induced osteoporosis, J. Bone Miner. Res. 35 (2020) 801–820, https://doi.org/10.1002/jbmr.3947.

[34] P. Li, B. Ji, H. Luo, D. Sundh, M. Lorentzon, J. Nielsen, One-year supplementation with Lactobacillus reuteri ATCC PTA 6475 counteracts a degradation of gut microbiota in older women with low bone mineral density, NPJ Biofilms Microbiomes 8 (2022) 84, https://doi.org/10.1038/s41522-022-00348-2.

[35] A.G. Nilsson, D. Sundh, F. Bäckhed, M. Lorentzon, Lactobacillus reuteri reduces bone loss in older women with low bone mineral density: a randomized, placebo-controlled, double-blind, clinical trial, J. Intern. Med. 284 (2018) 307–317, https://doi.org/10.1111/joim.12805.

[36] L. Tan, J. Fu, F. Feng, X. Liu, Z. Cui, B. Li, Y. Han, Y. Zheng, K.W.K. Yeung, Z. Li, S. Zhu, Y. Liang, X. Feng, X. Wang, S. Wu, Engineered probiotics biofilm enhances osseointegration via immunoregulation and anti-infection, Sci. Adv. 6 (2020) eaba5723, https://doi.org/10.1126/sciadv.aba5723.

[37] H. Gu, J. Fan, P. Bao, W. Qu, Z. Hu, B. Qi, X. Zhang, A. Yu, Probiotic biofilm modified 3D-printing scaffolds for improving chemo-immunotherapy of bone tumor and promoting osteogenesis, Adv. Funct. Mater. 34 (2024) 2311015, https://doi.org/10.1002/adfm.202311015.

[38] L. Davenport Huyer, S. Pascual-Gil, Y. Wang, S. Mandla, B. Yee, M. Radisic, Advanced strategies for modulation of the material–macrophage interface, Adv. Funct. Mater. 30 (2020) 1909331, https://doi.org/10.1002/adfm.201909331.

[39] Y. Zhu, H. Liang, X. Liu, J. Wu, C. Yang, T.M. Wong, K.Y.H. Kwan, K.M.C. Cheung, S. Wu, K.W.K. Yeung, Regulation of macrophage polarization through surface topography design to facilitate implant-to-bone osteointegration, Sci. Adv. 7 (2021), https://doi.org/10.1126/sciadv.abf6654 eabf6654.

[40] Q. Ma, L. Fang, N. Jiang, L. Zhang, Y. Wang, Y. Zhang, L. Chen, Bone mesenchymal stem cell secretion of sRANKL/OPG/M-CSF in response to macrophage-mediated inflammatory response influences osteogenesis on nanostructured Ti surfaces, Biomaterials 154 (2018) 234–247, https://doi.org/10.1016/j.biomaterials.2017.11.003.

[41] R. Zhang, T. Wang, Q. Lin, 847 Inflammasome activation in M2 macrophage restrain the immune suppressive function, in: Late-Breaking Abstracts, BMJ Publishing Group Ltd, 2020, https://doi.org/10.1136/jitc-2020-SITC2020.0847. A505–A505.

[42] B. Zhang, F. Han, Y. Wang, Y. Sun, M. Zhang, X. Yu, C. Qin, H. Zhang, C. Wu, Cells-micropatterning biomaterials for immune activation and bone regeneration, Adv. Sci. 9 (2022) 2200670, https://doi.org/10.1002/advs.202200670.

[43] M. Li, H. Ma, F. Han, D. Zhai, B. Zhang, Y. Sun, T. Li, L. Chen, C. Wu, Microbially catalyzed biomaterials for bone regeneration, Adv. Mater. 33 (2021) 2104829, https://doi.org/10.1002/adma.202104829.

[44] F. Bouchart, O. Vidal, J.-M. Lacroix, C. Spriet, S. Chamary, A. Brutel, J.-C. Hornez, 3D printed bioceramic for phage therapy against bone nosocomial infections, Mater Sci Eng C Mater Biol Appl 111 (2020) 110840, https://doi.org/10.1016/j.msec.2020.110840.

[45] B. Feng, M. Zhang, C. Qin, D. Zhai, Y. Wang, Y. Zhou, J. Chang, Y. Zhu, C. Wu, 3D printing of conch-like scaffolds for guiding cell migration and directional bone growth, Bioact. Mater. 22 (2023) 127–140, https://doi.org/10.1016/j.bioactmat.2022.09.014.

[46] B. Fang, P. Qiu, C. Xia, D. Cai, C. Zhao, Y. Chen, H. Wang, S. Liu, H. Cheng, Z. Tang, B. Wang, S. Fan, X. Lin, Extracellular matrix scaffold crosslinked with vancomycin for multifunctional antibacterial bone infection therapy, Biomaterials 268 (2021) 120603, https://doi.org/10.1016/j.biomaterials.2020.120603.

[47] X. Jing, C. Xu, W. Su, Q. Ding, B. Ye, Y. Su, K. Yu, L. Zeng, X. Yang, Y. Qu, K. Chen, T. Sun, Z. Luo, X. Guo, Photosensitive and conductive hydrogel induced innerved bone regeneration for infected bone defect repair, Adv. Healthcare Mater. 12 (2023) 2201349, https://doi.org/10.1002/adhm.202201349.

[48] I. Uiiah, L. Cao, W. Cui, Q. Xu, R. Yang, K. Tang, X. Zhang, Stereolithography printing of bone scaffolds using biofunctional calcium phosphate nanoparticles, J. Mater. Sci. Technol. 88 (2021) 99–108, https://doi.org/10.1016/j.jmst.2021.01.062.

[49] S. Jk, S. A, H. Eb, V. Sf, O. Pl, B. Ma, S. Dm, M. Ta, D. S, W. J, V. J, H. Sk, From prediction to function using evolutionary genomics: human-specific ecotypes of Lactobacillus reuteri have diverse probiotic functions, Genome Biology and Evolution 6 (2014), https://doi.org/10.1093/gbe/evu137.

[50] R.D. Shelby, G.E. Janzow, L. Mashburn-Warren, J. Galley, N. Tengberg, J. Navarro, M. Conces, M.T. Bailey, S.D. Goodman, G.E. Besner, A novel probiotic therapeutic in a murine model of Clostridioides difficile colitis, Gut Microb. 12 (2020) 1814119, https://doi.org/10.1080/19490976.2020.1814119.

[51] C. Depommier, A. Everard, C. Druart, H. Plovier, M. Van Hul, S. Vieira-Silva, G. Falony, J. Raes, D. Maiter, N.M. Delzenne, M. de Barsy, A. Loumaye, M. P. Hermans, J.-P. Thissen, W.M. de Vos, P.D. Cani, Supplementation with Akkermansia muciniphila in overweight and obese human volunteers: a proof-of-concept exploratory study, Nat Med 25 (2019) 1096–1103, https://doi.org/10.1038/s41591-019-0495-2.

[52] S.A. Strathdee, G.F. Hatfull, V.K. Mutalik, R.T. Schooley, Phage therapy: from biologic mechanisms to future directions, Cell 186 (2023) 17–31, https://doi.org/10.1016/j.cell.2022.11.017.

[53] X. Stachurska, K. Cendrowski, K. Pachnowska, A. Piegat, E. Mijowska, P. Nawrotek, Nanoparticles influence lytic phage T4-like performance in vitro, Int. J. Mol. Sci. 23 (2022) 7179, https://doi.org/10.3390/ijms23137179.

[54] S. O'Flaherty, R.P. Ross, W. Meaney, G.F. Fitzgerald, M.F. Elbreki, A. Coffey, Potential of the polyvalent anti-Staphylococcus bacteriophage K for control of antibiotic-resistant staphylococci from hospitals, Appl. Environ. Microbiol. 71 (2005) 1836–1842, https://doi.org/10.1128/AEM.71.4.1836-1842.2005.

[55] S. Abraham, Y. Kaufman, F. Perreault, R. Young, E. Bar-Zeev, Bursting out: linking changes in nanotopography and biomechanical properties of biofilm-forming Escherichia coli to the T4 lytic cycle, NPJ Biofilms Microbiomes 7 (2021) 26, https://doi.org/10.1038/s41522-021-00195-7.

[56] R.Y.K. Chang, S.C. Nang, H.-K. Chan, J. Li, Novel antimicrobial agents for combating antibiotic-resistant bacteria, Adv. Drug Deliv. Rev. 187 (2022) 114378, https://doi.org/10.1016/j.addr.2022.114378.

[57] Y. Zhang, Y. Cheng, Z. Zhao, S. Jiang, Y. Zhang, J. Li, S. Huang, W. Wang, Y. Xue, A. Li, Z. Tao, Z. Wu, X. Zhang, Enhanced chemoradiotherapy for MRSA-infected osteomyelitis using immunomodulatory polymer-reinforced nanotherapeutics, Adv. Mater. (2024) 2304991, https://doi.org/10.1002/adma.202304991.

[58] P.M.-K. Tang, D.J. Nikolic-Paterson, H.-Y. Lan, Macrophages: versatile players in renal inflammation and fibrosis, Nat. Rev. Nephrol. 15 (2019) 144–158, https://doi.org/10.1038/s41581-019-0110-2.

[59] Z.-J. Xu, Y. Gu, C.-Z. Wang, Y. Jin, X.-M. Wen, J.-C. Ma, L.-J. Tang, Z.-W. Mao, J. Qian, J. Lin, The M2 macrophage marker CD206: a novel prognostic indicator for acute myeloid leukemia, OncoImmunology 9 (2020) 1683347, https://doi.org/10.1080/2162402X.2019.1683347.

[60] G. Peng, W. Li, L. Peng, R. Li, Z. Wang, Y. Zhou, L. Gou, X. Zhu, Q. Xie, X. Zhang, S. Shen, L. Wu, L. Hu, C. Wang, X. Zheng, N. Tong, Multifunctional DNA-based hydrogel promotes diabetic alveolar bone defect reconstruction, Small 20 (2024) 2305594, https://doi.org/10.1002/smll.202305594.

[61] D.M. Musher, R.J. Arasaratnam, Contributions of animal studies to the understanding of infectious diseases, Clin. Infect. Dis. 74 (2022) 1872–1878, https://doi.org/10.1093/cid/ciab844.

[62] R.-X. Wu, C. Ma, Y. Liang, F.-M. Chen, X. Liu, ECM-mimicking nanofibrous matrix coaxes macrophages toward an anti-inflammatory phenotype: cellular behaviors and transcriptome analysis, Appl. Mater. Today 18 (2020) 100508, https://doi.org/10.1016/j.apmt.2019.100508.

[63] M. Li, A. Zhang, J. Li, J. Zhou, Y. Zheng, C. Zhang, D. Xia, H. Mao, J. Zhao, Osteoblast/fibroblast coculture derived bioactive ECM with unique matrisome profile facilitates bone regeneration, Bioact. Mater. 5 (2020) 938–948, https://doi.org/10.1016/j.bioactmat.2020.06.017.

[64] W. Zou, M. Xia, K. Jiang, Z. Cao, X. Zhang, X. Hu, Photo-oxidative degradation mitigated the developmental toxicity of polyamide microplastics to zebrafish larvae by modulating macrophage-triggered proinflammatory responses and apoptosis, Environ. Sci. Technol. 54 (2020) 13888–13898, https://doi.org/10.1021/acs.est.0c05399.

[65] Q. Yang, Z. Wang, C.H.H. Hor, H. Xiao, Z. Bian, J. Joelle Wang, Asymmetric synthesis of flavanols via Cu-catalyzed kinetic resolution of chromenes and their anti-inflammatory activity, Sci. Adv. 8 (2022) eabm9603, https://doi.org/10.1126/sciadv.abm9603.

[66] Y. Tian, Y. Li, J. Liu, Y. Lin, J. Jiao, B. Chen, W. Wang, S. Wu, C. Li, Photothermal therapy with regulated Nrf2/NF-κB signaling pathway for treating bacteria-induced periodontitis, Bioact. Mater. 9 (2022) 428–445, https://doi.org/10.1016/j.bioactmat.2021.07.033.

[67] X. Dong, H. Zhang, P. Duan, K. Liu, Y. Yu, W. Wei, W. Wang, Y. Liu, Q. Cheng, X. Liang, Y. Huo, L. Yan, A. Yu, H. Dai, An injectable and adaptable hydrogen sulfide delivery system for modulating neuroregenerative microenvironment, Sci. Adv. 9 (2023) eadi1078, https://doi.org/10.1126/sciadv.adi1078.

[68] Q. Guo, Y. Jin, X. Chen, X. Ye, X. Shen, M. Lin, C. Zeng, T. Zhou, J. Zhang, NF-κB in biology and targeted therapy: new insights and translational implications, Sig Transduct Target Ther 9 (2024) 1–37, https://doi.org/10.1038/s41392-024-01757-9.

[69] K.G. Burt, M.K.M. Kim, D.C. Viola, A.C. Abraham, N.O. Chahine, Nuclear factor κB overactivation in the intervertebral disc leads to macrophage recruitment and severe disc degeneration, Sci. Adv. 10 (2024) eadj3194, https://doi.org/10.1126/sciadv.adj3194.

[70] S. Ahn, M.H. Siddiqi, H.-Y. Noh, Y.-J. Kim, Y.-J. Kim, C.-G. Jin, D.-C. Yang, Anti-inflammatory activity of ginsenosides in LPS-stimulated RAW 264.7 cells, Sci. Bull. 60 (2015) 773–784, https://doi.org/10.1007/s11434-015-0773-4.

[71] M. Li, A. Zhang, J. Li, J. Zhou, Y. Zheng, C. Zhang, D. Xia, H. Mao, J. Zhao, Osteoblast/fibroblast coculture derived bioactive ECM with unique matrisome profile facilitates bone regeneration, Bioact. Mater. 5 (2020) 938–948, https://doi.org/10.1016/j.bioactmat.2020.06.017.

[72] S. Jin, X. Fu, W. Zeng, A. Chen, Z. Luo, Y. Li, Z. Zhou, J. Li, Chopped fibers and nano-hydroxyapatite enhanced silk fibroin porous hybrid scaffolds for bone augmentation, J. Mater. Chem. B 11 (2023) 1557–1567, https://doi.org/10.1039/D2TB02510H.

[73] P. Leucht, S. Lee, N. Yim, Wnt signaling and bone regeneration: can't have one without the other, Biomaterials 196 (2019) 46–50, https://doi.org/10.1016/j.biomaterials.2018.03.029.

[74] M. Wu, G. Chen, Y.-P. Li, TGF-β and BMP signaling in osteoblast, skeletal development, and bone formation, homeostasis and disease, Bone Res 4 (2016) 1–21, https://doi.org/10.1038/boneres.2016.9.

[75] J. Lei, C. Wang, X. Feng, L. Ma, X. Liu, Y. Luo, L. Tan, S. Wu, C. Yang, Sulfur-regulated defect engineering for enhanced ultrasonic piezocatalytic therapy of bacteria-infected bone defects, Chem. Eng. J. 435 (2022) 134624, https://doi.org/10.1016/j.cej.2022.134624.

[76] Y. Bian, T. Hu, K. Zhao, X. Cai, M. Li, C. Tan, R. Liang, X. Weng, A LDH-derived metal sulfide nanosheet-functionalized bioactive glass scaffold for vascularized osteogenesis and periprosthetic infection prevention/treatment, Adv. Sci. 11 (2024) 2403009, https://doi.org/10.1002/advs.202403009.

[77] C. Tang, D. Liang, Y. Qiu, J. Zhu, G. Tang, Omentin-1 induces osteoblast viability and differentiation via the TGF-β/Smad signaling pathway in osteoporosis, Mol. Med. Rep. 25 (2022) 132, https://doi.org/10.3892/mmr.2022.12648.